



The Abdus Salam
**International Centre
for Theoretical Physics**



The International Union of Geodesy and
Geophysics



2373-10

Workshop on Geophysical Data Analysis and Assimilation

29 October - 3 November, 2012

Methods of data assimilation in geodynamic models

Alik T. Ismail-Zadeh

*Karlsruhe Institute of Technology, Karlsruhe
Germany*

*Institute of Earthquake Prediction Theory and Mathematical Geophysics, RAS, Moscow
Russia*

*Institut de Physique du Globe de Paris, Paris
France*

**WORKSHOP ON GEOPHYSICAL DATA
ANALYSIS AND ASSIMILATION**

29 October 2012 - 3 November 2012

Methods of data assimilation in geodynamic models

Alik T. Ismail-Zadeh

Institute of Applied Geosciences, Karlsruhe Institute of Technology,
Karlsruhe, Germany

Institute of Earthquake Prediction Theory and Mathematical Geophysics,
Russian Academy of Sciences, Moscow, Russia

Institut de Physique du Globe de Paris,
Paris, France

TRIESTE
October 2012

8.1 Introduction

Many geodynamic problems can be described by mathematical models, i.e. by a set of partial differential equations and boundary and/or initial conditions defined in a specific domain. A mathematical model links the causal characteristics of a geodynamic process with its effects. The causal characteristics of the process include, for example, parameters of the initial and boundary conditions, coefficients of the differential equations, and geometrical parameters of a model domain. The aim of the *direct* mathematical problem is to determine the relationship between the causes and effects of the geodynamic process and hence to find a solution to the mathematical problem for a given set of parameters and coefficients. An *inverse* problem is the opposite of a direct problem. An inverse problem is considered when there is a lack of information on the causal characteristics (but information on the effects of the geodynamic process exists). Inverse problems can be subdivided into time-reverse or retrospective problems (e.g. to restore the development of a geodynamic process), coefficient problems (e.g. to determine the coefficients of the model equations and/or boundary conditions), geometrical problems (e.g. to determine the location of heat sources in a model domain or the geometry of the model boundary), and some others. In this chapter we will consider time-reverse (retrospective) problems in geodynamics.

Inverse problems are often ill-posed. *Jacques Hadamard* (1865–1963) introduced the idea of well- (and ill-) posed problems in the theory of partial differential equations (Hadamard, 1902). A mathematical model for a geophysical problem has to be well-posed in the sense that it has to have the properties of existence, uniqueness and stability of a solution to the problem. Problems for which at least one of these properties does not hold are called ill-posed. The requirement of stability is the most important one. If a problem lacks the property of stability then its solution is almost impossible to compute because computations are polluted by unavoidable errors. If the solution of a problem does not depend continuously on the initial data, then, in general, the computed solution may have nothing to do with the true solution.

The inverse (retrospective) problem of thermal convection in the mantle is an ill-posed problem, since the backward heat problem, describing both heat advection and conduction through the mantle backwards in time, possesses the properties of ill-posedness (Kirsch, 1996). In particular, the solution to the problem does not depend continuously on the initial data. This means that small changes in the present-day temperature field may result in large changes of predicted mantle temperatures in the past. Let us explain this statement in the case of the one-dimensional (1-D) diffusion equation.

Consider the following boundary-value problem for the 1-D backward diffusion equation:

$$\partial u(t, x) / \partial t = \partial^2 u(t, x) / \partial x^2, \quad 0 \leq x \leq \pi, \quad t \leq 0 \quad (8.1)$$

with the following boundary and initial conditions

$$u(t, 0) = 0 = u(t, \pi), \quad t \leq 0, \quad (8.2)$$

$$u(0, x) = \phi_n(x), \quad 0 \leq x \leq \pi. \quad (8.3)$$

At the initial time we assume that the function $\phi_n(x)$ takes the following two forms:

$$\phi_n(x) = \frac{\sin((4n+1)x)}{4n+1} \quad (8.4)$$

and

$$\phi_0(x) \equiv 0. \quad (8.5)$$

Note that

$$\max_{0 \leq x \leq \pi} |\phi_n(x) - \phi_0(x)| \leq \frac{1}{4n+1} \rightarrow 0 \quad \text{at } n \rightarrow \infty. \quad (8.6)$$

The following two solutions of the problem correspond to the two chosen functions of $\phi_n(x)$, respectively:

$$u_n(t, x) = \frac{\sin((4n+1)x)}{4n+1} \exp(-(4n+1)^2 t) \quad \text{at } \phi_n(x) = \phi_n \quad (8.7)$$

and

$$u_0(t, x) \equiv 0 \quad \text{at } \phi_n(x) = \phi_0. \quad (8.8)$$

At $t = -1$ and $x = \pi/2$ we obtain

$$u_n(-1, \pi/2) = \frac{1}{4n+1} \exp((4n+1)^2) \quad \text{at } n \rightarrow \infty. \quad (8.9)$$

At large n two closely set initial functions ϕ_n and ϕ_0 are associated with the two strongly different solutions at $t = -1$ and $x = \pi/2$. Hence, a small error in the initial data (8.6) can result in very large errors in the solution to the backward problem (8.9), and therefore the solution is unstable, and the problem is ill-posed.

Despite the fact that many inverse problems are ill-posed, there are methods for solving the problems. *Andrei Tikhonov* (1906–1993) introduced the idea of conditionally well-posed problems and the regularisation method (Tikhonov, 1963). According to Tikhonov, a class of admissible solutions to conditionally ill-posed problems should be selected to satisfy the following conditions: (i) a solution exists in this class, (ii) the solution is unique in the same class and (iii) the solution depends continuously on the input data. The Tikhonov

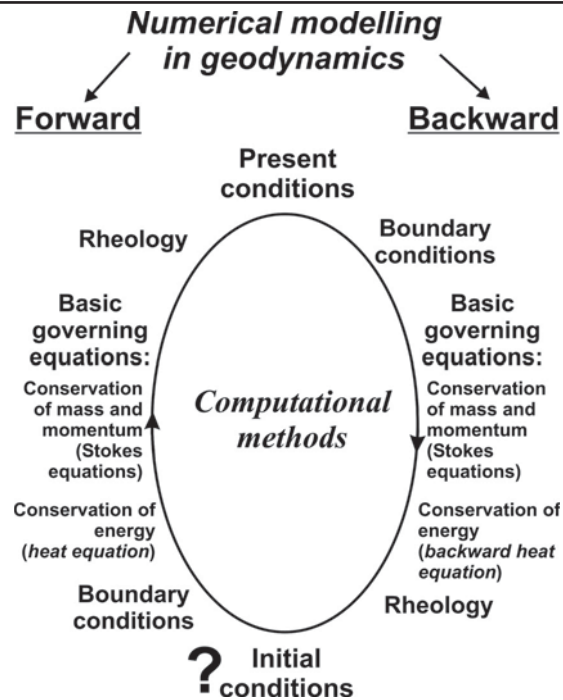


Fig. 8.1.

Flowchart of forward and backward numerical modelling in geodynamics.

regularisation is essentially a trade-off between fitting the observations and reducing a norm of the solution to the mathematical model of a geophysical problem.

Forward modelling in geodynamics is associated with the solution of direct mathematical problems, and *backward modelling* with the solution of inverse (time-reverse) problems. Figure 8.1 illustrates the flow in forward and backward numerical modelling. In forward modelling one starts with unknown initial conditions, which are added to a set of governing equations, rheological law and boundary conditions to define properly the relevant mathematical problem. Once the problem is stated, a numerical model (a set of discrete equations) is solved forward in time using computational methods. The initial conditions of the numerical model vary (keeping all other model parameters unchanged) to fit model results to reality (present observations). Because the model depends on the initial conditions and they are unknown *a priori*, the task 'to fit model results to reality' becomes difficult.

Another approach is to use backward modelling. In this case present observations are employed as input conditions for the mathematical model. We shall use the term of 'input conditions' in backward modelling to distinguish it from the term of 'initial conditions' for the forward modelling, although the 'input conditions' are the initial conditions for the mathematical model in backward modelling. The aim of backward modelling in geodynamics is to find the 'initial conditions' in the geological past from the present observations and to restore mantle structures accordingly. Special methods are required to assimilate present observations to the past (Ismail-Zadeh *et al.*, 2009). In the following sections we describe the methods for data assimilation.

8.2 Data assimilation

The mantle is heated from the core and from inside owing to decay of radioactive elements. Since thermal convection in the mantle is described by heat advection and diffusion, one can ask: is it possible to tell, from the present temperature distribution estimations of the Earth, something about the Earth's temperature distribution in the geological past? Even though heat diffusion is irreversible in the physical sense, it is possible to predict accurately the heat transfer backwards in time by using data assimilation techniques without contradicting the basic thermodynamic laws (see, for example, Ismail-Zadeh *et al.*, 2004a, 2007).

To restore mantle dynamics in the geological past, data assimilation techniques can be used to constrain the initial conditions for the mantle temperature and velocity from their present observations. The initial conditions so obtained can then be used to run forward models of mantle dynamics to restore the evolution of mantle structures. *Data assimilation* can be defined as the incorporation of observations (in the present) and initial conditions (in the past) in an explicit dynamic model to provide time continuity and coupling among the physical fields (e.g. velocity, temperature). The basic principle of data assimilation is to consider the initial condition as a control variable and to optimise the initial condition in order to minimise the discrepancy between the observations and the solution of the model.

If heat diffusion is neglected, the present mantle temperature and flow can be assimilated into the past by using the backward advection (BAD). Numerical approaches to the solution of the inverse problem of the Rayleigh–Taylor instability were developed for a dynamic restoration of diapiric structures to their earlier stages (Ismail-Zadeh *et al.*, 2001b; Kaus and Podladchikov, 2001; Korotkii *et al.*, 2002; Ismail-Zadeh *et al.*, 2004b). Steinberger and O'Connell (1998) and Conrad and Gurnis (2003) modelled the mantle flow backwards in time from present-day mantle density heterogeneities inferred from seismic observations.

In sequential filtering a numerical model is computed forward in time for the interval for which observations have been made, updating the model each time where observations are available. The sequential filtering was used to compute mantle circulation models (Bunge *et al.*, 1998, 2002). Despite sequential data assimilation well adapted to mantle circulation studies, each individual observation influences the model state at later times. Information propagates from the geological past into the future, although our knowledge of the Earth's mantle at earlier times is much poorer than that at present.

The variational (VAR) data assimilation method has been pioneered by meteorologists and used very successfully to improve operational weather forecasts (see Kalnay, 2003). The data assimilation has also been widely used in oceanography (see Bennett, 1992) and in hydrological studies (see McLaughlin, 2002). The use of VAR data assimilation in models of mantle dynamics (to estimate mantle temperature and flow in the geological past) has been put forward by Bunge *et al.* (2003) and Ismail-Zadeh *et al.* (2003a, b) independently. The major differences between the two approaches are that Bunge *et al.* (2003) applied the VAR method to the coupled Stokes, continuity and heat equations (generalised inverse), whereas Ismail-Zadeh *et al.* (2003a) applied the VAR method to the heat equation only. The VAR approach by Ismail-Zadeh *et al.* (2003a) is computationally less expensive, because

it does not involve the Stokes equation in the iterations between the direct and adjoint problems. Moreover, this approach admits the use of temperature-dependent viscosity.

The VAR data assimilation algorithm was employed for numerical restoration of models of present prominent mantle plumes to their past stages (Ismail-Zadeh *et al.*, 2004a; Hier-Majumder *et al.*, 2005). Effects of thermal diffusion and temperature-dependent viscosity on the evolution of mantle plumes was studied by Ismail-Zadeh *et al.* (2006) to recover the structure of mantle plumes prominent in the past from that of present plumes weakened by thermal diffusion. Liu and Gurnis (2008) simultaneously inverted mantle properties and initial conditions using the VAR data assimilation method and applied the method to reconstruct the evolution of the Farallon Plate subduction (Liu *et al.*, 2008).

The quasi-reversibility (QRV) method was introduced by Lattes and Lions (1969). The use of the QRV method implies the introduction into the backward heat equation of the additional term involving the product of a small regularisation parameter and a higher-order temperature derivative. The data assimilation in this case is based on a search of the best fit between the forecast model state and the observations by minimising the regularisation parameter. The QRV method was introduced in geodynamic modelling (Ismail-Zadeh *et al.*, 2007) and employed to assimilate data in models of mantle dynamics (Ismail-Zadeh *et al.*, 2008).

In this chapter we describe three principal techniques used to assimilate data related to geodynamics: (i) backward advection, (ii) variational (adjoint) and (iii) quasi-reversibility methods.

8.3 Backward advection (BAD) method

We consider the three-dimensional model domain $\Omega = [0, x_1 = 3h] \times [0, x_2 = 3h] \times [0, x_3 = h]$, where $\mathbf{x} = (x_1, x_2, x_3)$ are the Cartesian coordinates and h is the depth of the domain, and assume that the mantle behaves as a Newtonian incompressible fluid with a temperature-dependent viscosity and infinite Prandtl number. The mantle flow is described by heat, motion and continuity equations (Chandrasekhar, 1961). To simplify the governing equations, we make the Boussinesq approximation (Boussinesq, 1903) keeping the density constant everywhere except for buoyancy term in the equation of motion. In the Boussinesq approximation the dimensionless equations take the form:

$$\partial T / \partial t + \mathbf{u} \cdot \nabla T = \nabla^2 T, \quad \mathbf{x} \in \Omega, \quad t \in (0, \vartheta), \quad (8.10)$$

$$\nabla P = \text{div} [\eta \mathbf{E}] + Ra T \mathbf{e}, \quad \mathbf{E} = \{\partial u_i / \partial x_j + \partial u_j / \partial x_i\}, \quad \mathbf{e} = (0, 0, 1), \quad (8.11)$$

$$\text{div} \mathbf{u} = 0, \quad t \in (0, \vartheta), \quad \mathbf{x} \in \Omega. \quad (8.12)$$

Here T , t , $\mathbf{u} = (u_1, u_2, u_3)$, P and η are dimensionless temperature, time, velocity, pressure and viscosity, respectively. The Rayleigh number is defined as $Ra = \alpha g \rho_{ref} \Delta T h^3 \eta_{ref}^{-1} \kappa^{-1}$, where α is the thermal expansivity, g is the acceleration due to gravity, ρ_{ref} and η_{ref} are the reference typical density and viscosity, respectively; ΔT is the temperature contrast between

the lower and upper boundaries of the model domain; and κ is the thermal diffusivity. In Eqs. (8.10)–(8.12) length, temperature and time are normalised by h , ΔT and $h^2\kappa^{-1}$, respectively.

At the boundary Γ of the model domain Ω we set the impenetrability condition with no-slip or perfect slip conditions: $\mathbf{u} = 0$ or $\partial\mathbf{u}_\tau/\partial\mathbf{n} = 0$, $\mathbf{u} \cdot \mathbf{n} = 0$, where \mathbf{n} is the outward unit normal vector at a point on the model boundary, and \mathbf{u}_τ is the projection of the velocity vector onto the tangent plane at the same point on the model boundary. We assume zero heat flux through the vertical boundaries of the box. Either temperature or heat flux are prescribed at the upper and lower boundaries of the model domain. To solve the problem forward or backward in time we assume the temperature to be known at the initial time ($t = 0$) or at the present time ($t = \vartheta$). Equations (8.10)–(8.12) together with the boundary and initial conditions describe a thermo-convective mantle flow.

The principal difficulty in solving the problem (8.10)–(8.12) backward in time is the ill-posedness of the backward heat problem and the presence of the heat diffusion term in the heat equation. The backward advection (BAD) method suggests neglecting the heat diffusion term, and the heat advection equation can then be solved backward in time. Both direct (forward in time) and inverse (backward in time) problems of the heat (density) advection are well-posed. This is because the time-dependent advection equation has the same form of characteristics for the direct and inverse velocity field (the vector velocity reverses its direction, when time is reversed). Therefore, numerical algorithms used to solve the direct problem of the gravitational instability can also be used in studies of the time-reverse problems by replacing positive time steps with negative ones.

Using the BAD method, Steinberger and O'Connell (1998) studied the motion of hotspots relative to the deep mantle. They combined the advection of plumes, which are thought to cause the hotspots on the Earth's surface, with a large-scale mantle flow field and constrained the viscosity structure of the Earth's mantle. Conrad and Gurnis (2003) modelled the history of mantle flow by using a tomographic image of the mantle beneath southern Africa as an input (initial) condition for the backward mantle advection model while reversing the direction of flow. If the resulting model of the evolution of thermal structures obtained by the BAD method is used as a starting point for a forward mantle convection model, present mantle structures can be reconstructed if the time of assimilation does not exceed 50–75 Myr.

8.4 Application of the BAD method: restoration of the evolution of salt diapirs

Salt is so buoyant and weak compared with most other rocks with which it is found that it develops distinctive structures with a wide variety of shapes and relationships with other rocks by various combinations of gravity, thermal effects and lateral forces. The crests of passive salt bodies can stay near the sedimentation surface while their surroundings are buried (downbuilt) by other sedimentary rocks (Jackson *et al.*, 1994). The profiles of downbuilt passive diapirs can simulate those of fir trees because they reflect the ratio of increase in diapir height relative to the rate of accumulation of the downbuilding sediments (Talbot, 1995) and lateral forces (Koyi, 1996). Salt movements can be triggered by faulting and

driven by erosion and redeposition, differential loading, buoyancy and other geological processes. Many salt sequences are buried by overburdens sufficiently stiff to resist the buoyancy of the salt. Such salt will only be driven by differential loading into sharp-crested reactive-diapiric walls after the stiff overburden is weakened and thinned by faults (Vendeville and Jackson, 1992). Such reactive diapirs often rise up and out of the fault zone and thereafter can continue increasing in relief as by passive downbuilding of more sediment.

Active diapirs are those that lift or displace their overburdens. Although any erosion of the crests of salt structures and deposition of surrounding overburden rocks influence their growth, diapirs with significant relief have sufficient buoyancy to rise (upbuild) through stiff overburdens (Jackson *et al.*, 1994). The rapid deposition of denser and more viscous sediments over less dense and viscous salt results in the Rayleigh–Taylor instability. This leads to a gravity-driven single overturn of the salt layer with its denser but ductile overburden. Rayleigh–Taylor overturns (Ramberg, 1968) are characterised by the rise of rock salt through overlying and younger compacting clastic sediments that are deformed as a result. The consequent salt structures evolve through a great variety of shapes. Perturbations of the interface between salt and its denser overburden result in the overburden subsiding as salt rises owing to the density inversion.

Two-dimensional (2-D) numerical models of salt diapirism were first developed by Woitd (1978) who examined how the viscosity ratio between the salt and its overburden affects the shapes and growth rate of diapirs. Schmeling (1987) demonstrated how the dominant wavelength and the geometry of gravity overturns are influenced by the initial shape of the interface between the salt and its overburden. Römer and Neugebauer (1991) presented numerical results of modelling diapiric structures in a multilayered medium. Later Poliakov *et al.* (1993a) and Naimark *et al.* (1998) developed numerical models of diapiric growth considering the effects of sedimentation and redistribution of sediments. Van Keken *et al.* (1993), Poliakov *et al.* (1993b), Daudre and Cloetingh (1994), and Poliakov *et al.* (1996) introduced non-linear rheological properties of salt and overburden into their numerical models. The authors mentioned above used various numerical methods to compute the models of salt diapirism, among them FD method, Lagrangian and Eulerian FE method and their combination.

Two-dimensional analyses of the evolution of salt structures are restricted and not suitable for examining the complicated shapes of mature diapiric patterns. Resolving the geometry of gravity overturns requires three-dimensional (3-D) numerical modelling. Ismail-Zadeh *et al.* (2000b) analysed such typical 3-D structures as deep polygonal buoyant ridges, shallow salt-stock canopies and salt walls. Kaus and Podladchikov (2001) showed how complicated 3-D diapirs developed from initial 2-D perturbations of the interface between salt and its overburden.

The increasing application of 3-D seismic exploration in oil and gas prospecting points to the need for vigorous efforts toward numerical modelling of the evolution of salt structures in three dimensions, both forward and backward in time. Most numerical models of salt diapirism involved the forward evolution of salt structures toward increasing maturity. Ismail-Zadeh *et al.* (2001b) developed a numerical approach to 2-D dynamic restoration of cross-sections across salt structures. The approach was based on solving the inverse problem of gravitational instability by the BAD method. The same method was used in

3-D cases to model Rayleigh-Taylor instability backward in time (Kaus and Podladchikov, 2001; Korotkii *et al.*, 2002; Ismail-Zadeh *et al.*, 2004b).

We consider here the advection problem (slow flow of an incompressible fluid of variable density and viscosity due to gravity) in the rectangular domain Ω . A 3-D model of the flow of salt and of the viscous deformation of the overburden of salt is described by the Stokes equations (8.11), where the term $Ra T$ is replaced by the term $-g\rho$, and by Eq. (8.10), where temperature T is replaced by density ρ (viscosity η) and the term on the right-hand side is omitted. Equation (8.10) in this case describes the advection of density (viscosity) with the flow. For details of the numerical model see Section 4.10.2.

Although dimensionless values and functions are used in computations, numerical results are presented in dimensional form for the reader's convenience. The time step Δt is chosen from the condition that the maximum displacement does not exceed a given small value h : $\Delta t = h/u_{\max}$, where u_{\max} is the maximum value of the flow velocity. Salt diapirs in the numerical model evolve from random initial perturbations of the interface between the salt and its overburden deposited on the top of horizontal salt layer prior to the interface perturbation. Initially the evolution of salt diapirs is modelled forward in time as presented in the model example in Section 4.10.2. Figures 8.2 (a–d, a front view) and 8.3 (a–d, a top view) show the positions of the interface between salt and overburden in the model at successive times over a period of about 21 Myr.

To restore the evolution of salt diapirs predicted by the forward model through successive earlier stages, a positive time is replaced by a negative time, and the problem is solved backward in time. Such a replacement is possible, because the characteristics of the advection equations have the same form for both direct and inverse velocity fields. The final position of the interface between salt and its overburden in the forward model (Figs. 8.2d and 8.3d) is used as an initial position of the interfaces for the backward model. Figures 8.2, d–g and 8.3, d–g illustrate successive steps in the restoration of the upbuilt diapirs. Least square errors δ of the restoration are calculated by using the formula:

$$\delta(x_1, x_2) = \left(\int_0^h (\rho(x_1, x_2, x_3) - \tilde{\rho}(x_1, x_2, x_3))^2 dx_3 \right)^{1/2}, \quad (8.13)$$

where $\rho(x_1, x_2, x_3)$ is the density at initial time, and $\tilde{\rho}(x_1, x_2, x_3)$ is the restored density (Fig. 8.3h). The maximum value δ does not exceed 120 kg m^{-3} , and the error is associated with small areas of the initial interface's perturbation.

To demonstrate the stability of the restoration results with respect to changes in the density of the overburden, the restoration procedure was tested by synthetic examples. Initially the forward model is run for 200 computational time steps (about 30 Myr). Then the density contrast ($\delta\rho$) between salt and its overburden is changed by a few per cent: namely, $\delta\rho$ was chosen to be 400, 405, 410 (the actual contrast), 415 and 420 kg m^{-3} . The evolution of the system was restored for these density contrasts. Ismail-Zadeh *et al.* (2004b) found small discrepancies (less than 0.5%) between least square errors for all these test cases. The tests show that the solution is stable to small changes in the initial conditions, and this is in agreement with the mathematical theory of well-posed problems (Tikhonov and

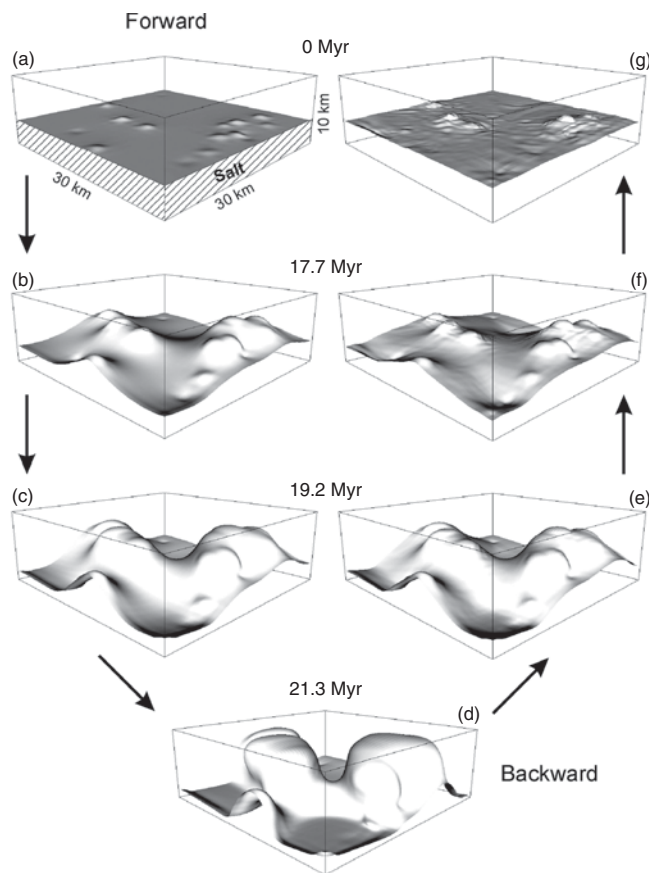


Fig. 8.2. Evolution (front view) of salt diapirs toward increasing maturity (a)–(d) and restoration of the evolution (d)–(g). Interfaces between salt and its overburden are presented at successive times. After Ismail-Zadeh *et al.* (2004b).

Samarskii, 1990). Meanwhile it should be mentioned that if the model is computed for a very long time and the less dense salt layer spreads uniformly into a horizontal layer near the surface, practical restoration of the layered structure becomes impossible (Ismail-Zadeh *et al.*, 2001b).

8.5 Variational (VAR) method

In this section we describe a variational approach to numerical restoration of thermoconvective mantle flow. The variational data assimilation is based on a search of the best fit between the forecast model state and the observations by minimising an objective functional (a normalised residual between the target model and observed variables) over space

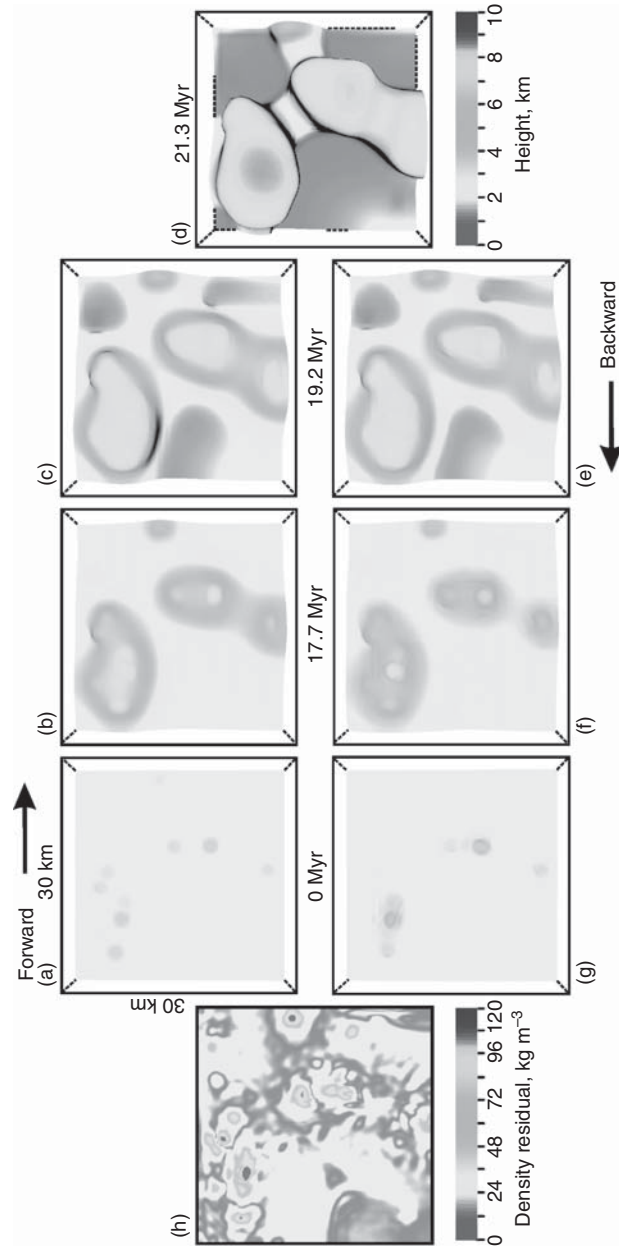


Fig. 8.3. Evolution (top view) of salt diapirs toward increasing maturity (a)–(d) and restoration of the evolution (d)–(g) at the same times as in Fig. 8.2. (h) Restoration errors. After Ismail-Zadeh *et al.* (2004b). (In colour as Plate 2. See colour plates section.)

and time. To minimise the objective functional over time, an assimilation time interval is defined and an adjoint model is typically used to find the derivatives of the objective functional with respect to the model states. The variational data assimilation is well suited for smooth problems (we discuss the problem of smoothness in Section 8.7).

The method for variational data assimilation can be formulated with a weak constraint (a generalised inverse) where errors in the model formulation are taken into account (Bunge *et al.*, 2003) or with a strong constraint where the model is assumed to be perfect except for the errors associated with the initial conditions (Ismail-Zadeh *et al.*, 2003a). Actually there are several sources of errors in forward and backward modelling of thermo-convective mantle flow, which we discuss in Section 8.12. The generalised inverse of mantle convection considers model errors, data misfit and the misfit of parameters as control variables. Unfortunately the generalised inverse presents a tremendous computational challenge and is difficult to solve in practice. Hence, Bunge *et al.* (2003) considered a simplified generalised inverse imposing a strong constraint on errors (ignoring all errors except for the initial condition errors). Therefore, the strong constraint makes the problem computationally tractable.

We consider the following objective functional at $t \in [0, \vartheta]$

$$J(\varphi) = \|T(\vartheta, \cdot; \varphi) - \chi(\cdot)\|^2, \quad (8.14)$$

where $\|\cdot\|$ denotes the norm in the space $L_2(\Omega)$ (the Hilbert space with the norm defined as $\|y\| = [\int_{\Omega} y^2(\mathbf{x}) d\mathbf{x}]^{1/2}$). Since in what follows the dependence of solutions of the thermal boundary value problems on initial data is important, we introduce these data explicitly into the mathematical representation of temperature. Here $T(\vartheta, \cdot; \varphi)$ is the solution of the thermal boundary value problem (8.10) at the final time ϑ , which corresponds to some (unknown as yet) initial temperature distribution $\varphi(\mathbf{x})$; $\chi(\mathbf{x}) = T(\vartheta, \mathbf{x}; T_0)$ is the known temperature distribution at the final time, which corresponds to the initial temperature $T_0(\cdot)$. The functional has its unique global minimum at value $\varphi \equiv T_0$ and $J(T_0) \equiv 0$, $\nabla J(T_0) \equiv 0$ (Vasiliev, 2002).

To find the minimum of the functional we employ the gradient method ($k = 0, \dots, j, \dots$):

$$\varphi_{k+1} = \varphi_k - \beta_k \nabla J(\varphi_k), \quad \varphi_0 = T_*, \quad (8.15)$$

$$\beta_k = \begin{cases} J(\varphi_k) / \|\nabla J(\varphi_k)\|, & 1 \leq k \leq k_* \\ 1/(k+1), & k > k_* \end{cases}, \quad (8.16)$$

where T_* is an initial temperature guess. The minimisation method belongs to a class of limited-memory quasi-Newton methods (Zou *et al.*, 1993), where approximations to the inverse Hessian matrices are chosen to be the identity matrix. Equation (8.16) is used to maintain the stability of the iteration scheme (8.15). Consider that the gradient of the objective functional $\nabla J(\varphi_k)$ is computed with an error $\|\nabla J_{\delta}(\varphi_k) - \nabla J(\varphi_k)\| < \delta$, where $\nabla J_{\delta}(\varphi_k)$ is the computed value of the gradient. We introduce the function $\varphi^{\infty} = \varphi_0 - \sum_{k=1}^{\infty} \beta_k \nabla J(\varphi_k)$, assuming that the infinite sum exists, and the function $\varphi_{\delta}^{\infty} = \varphi_0 - \sum_{k=1}^{\infty} \beta_k \nabla J_{\delta}(\varphi_k)$ as the computed value of φ^{∞} . For stability of the iteration method (8.15),

the following inequality should be held:

$$\begin{aligned} \|\varphi_\delta^\infty - \varphi^\infty\| &= \left\| \sum_{k=1}^{\infty} \beta_k (\nabla J_\delta(u_k) - \nabla J(u_k)) \right\| \\ &\leq \sum_{k=1}^{\infty} \beta_k \|\nabla J_\delta(\varphi_k) - \nabla J(\varphi_k)\| \leq \delta \sum_{k=1}^{\infty} \beta_k. \end{aligned}$$

The sum $\sum_{k=1}^{\infty} \beta_k$ is finite, if $\beta_k = 1/k^p$, $p > 1$. We use $p = 1$, but the number of iterations is limited, and therefore, the iteration method is conditionally stable, although the convergence rate of these iterations is low. Meanwhile the gradient of the objective functional $\nabla J(\varphi_k)$ decreases steadily with the number of iterations providing the convergence, although the absolute value of $J(\varphi_k)/\|\nabla J(\varphi_k)\|$ increases with the number of iterations, and it can result in instability of the iteration process (Samarskii and Vabischevich, 2004).

The minimisation algorithm requires the calculation of the gradient of the objective functional, ∇J . This can be done through the use of the *adjoint* problem for the model equations (8.10)–(8.12) with the relevant boundary and initial conditions. In the case of the heat problem, the adjoint problem can be represented in the following form:

$$\begin{aligned} \partial \Psi / \partial t + \mathbf{u} \cdot \nabla \Psi + \nabla^2 \Psi &= 0, & \mathbf{x} \in \Omega, t \in (0, \vartheta), \\ \sigma_1 \Psi + \sigma_2 \partial \Psi / \partial \mathbf{n} &= 0, & \mathbf{x} \in \Gamma, t \in (0, \vartheta), \\ \Psi(\vartheta, \mathbf{x}) &= 2(T(\vartheta, \mathbf{x}; \varphi) - \chi(\mathbf{x})), & \mathbf{x} \in \Omega, \end{aligned} \quad (8.17)$$

where σ_1 and σ_2 are some smooth functions or constants satisfying the condition $\sigma_1^2 + \sigma_2^2 \neq 0$. Selecting σ_1 and σ_2 we can obtain corresponding boundary conditions.

The solution to the adjoint problem (8.17) is the gradient of the objective functional (8.14). To prove the statement, we consider an increment of the functional J in the following form:

$$\begin{aligned} J(\varphi + h) - J(\varphi) &= \int_{\Omega} (T(\vartheta, \mathbf{x}; \varphi + h) - \chi(\mathbf{x}))^2 d\mathbf{x} - \int_{\Omega} (T(\vartheta, \mathbf{x}; \varphi) - \chi(\mathbf{x}))^2 d\mathbf{x} \\ &= 2 \int_{\Omega} (T(\vartheta, \mathbf{x}; \varphi) - \chi(\mathbf{x})) \zeta(\vartheta, \mathbf{x}) d\mathbf{x} + \int_{\Omega} \zeta^2(\vartheta, \mathbf{x}) d\mathbf{x} \\ &= \int_{\Omega} \Psi(\vartheta, \mathbf{x}) \zeta(\vartheta, \mathbf{x}) d\mathbf{x} + \int_{\Omega} \zeta^2(\vartheta, \mathbf{x}) d\mathbf{x} \\ &= \int_{\Omega} \int_0^{\vartheta} \frac{\partial}{\partial t} (\Psi(t, \mathbf{x}) \zeta(t, \mathbf{x})) d\mathbf{x} dt + \int_{\Omega} \Psi(0, \mathbf{x}) h(\mathbf{x}) d\mathbf{x} + \int_{\Omega} \zeta^2(\vartheta, \mathbf{x}) d\mathbf{x}, \end{aligned} \quad (8.18)$$

where $\Psi(t, \mathbf{x}) = 2(T(t, \mathbf{x}; \vartheta) - \chi(\mathbf{x}))$; $h(\mathbf{x})$ is a small heat increment to the unknown initial temperature $\varphi(\mathbf{x})$; and $\zeta = T(t, \mathbf{x}; \varphi + h) - T(t, \mathbf{x}; \varphi)$ is the solution to the following forward

heat problem

$$\begin{aligned}\partial\zeta/\partial t + \mathbf{u} \cdot \nabla\zeta - \nabla^2\zeta &= 0, & \mathbf{x} \in \Omega, t \in (0, \vartheta), \\ \sigma_1\zeta + \sigma_2\partial\zeta/\partial\mathbf{n} &= 0, & \mathbf{x} \in \Gamma, t \in (0, \vartheta), \\ \zeta(0, \mathbf{x}) &= h(\mathbf{x}), & \mathbf{x} \in \Omega.\end{aligned}\tag{8.19}$$

Considering the fact that $\Psi = \Psi(t, \mathbf{x})$ and $\zeta = \zeta(t, \mathbf{x})$ are the solutions to (8.17) and (8.19) respectively, and the velocity \mathbf{u} satisfies (8.12) and the boundary conditions specified, we obtain

$$\begin{aligned}\int_{\Omega} \int_0^{\vartheta} \frac{\partial}{\partial t} (\Psi(t, \mathbf{x})\zeta(t, \mathbf{x})) dt d\mathbf{x} &= \int_0^{\vartheta} \int_{\Omega} \left\{ \frac{\partial}{\partial t} \Psi(t, \mathbf{x})\zeta(t, \mathbf{x}) + \Psi(t, \mathbf{x}) \frac{\partial\zeta(t, \mathbf{x})}{\partial t} \right\} d\mathbf{x} dt \\ &= \int_0^{\vartheta} \int_{\Omega} \zeta(t, \mathbf{x}) [-\mathbf{u} \cdot \nabla\Psi - \nabla^2\Psi] d\mathbf{x} dt + \int_0^{\vartheta} \int_{\Omega} \Psi(t, \mathbf{x}) [-\mathbf{u} \cdot \nabla\zeta + \nabla^2\zeta] d\mathbf{x} dt \\ &= \int_0^{\vartheta} \int_{\Gamma} \{\Psi\nabla\zeta \cdot \mathbf{n} - \zeta\nabla\Psi \cdot \mathbf{n}\} d\Gamma dt + \int_0^{\vartheta} \int_{\Omega} \{\nabla\Psi \cdot \nabla\zeta - \nabla\zeta \cdot \nabla\Psi\} d\mathbf{x} dt \\ &\quad + \int_0^{\vartheta} \int_{\Omega} \{\zeta\Psi\nabla \cdot \mathbf{u} + \Psi\mathbf{u} \cdot \nabla\zeta - \Psi\mathbf{u} \cdot \nabla\zeta\} d\mathbf{x} dt - 2 \int_0^{\vartheta} \int_{\Gamma} \zeta\Psi\mathbf{u} \cdot \mathbf{n} d\Gamma dt = 0.\end{aligned}\tag{8.20}$$

Hence

$$J(\varphi + h) - J(\varphi) = \int_{\Omega} \Psi(0, \mathbf{x})h(\mathbf{x})d\mathbf{x} + \int_{\Omega} \zeta^2(\vartheta, \mathbf{x})d\mathbf{x} = \int_{\Omega} \Psi(0, \mathbf{x})h(\mathbf{x})d\mathbf{x} + o(\|h\|).\tag{8.21}$$

The gradient is derived by using the Gateaux derivative of the objective functional. Therefore, we obtain that the gradient of the functional is represented as

$$\nabla J(\varphi) = \Psi(0, \cdot).\tag{8.22}$$

Thus, the solution of the backward heat problem is reduced to solutions of series of forward problems, which are known to be well-posed (Tikhonov and Samarskii, 1990). The algorithm can be used to solve the problem over any subinterval of time in $[0, \vartheta]$.

We note that information on the properties of the Hessian matrix ($\nabla^2 J$) is important in many aspects of minimisation problems (Daescu and Navon, 2003). To obtain sufficient conditions for the existence of the minimum of the problem, the Hessian matrix must be positive definite at T_0 (optimal initial temperature). However, an explicit evaluation of the Hessian matrix in many cases is prohibitive owing to the number of variables.

We now describe the algorithm for numerical solution of the inverse problem of mantle convection, that is, the numerical algorithm to solve (8.10)–(8.12) backward in time using the VAR method. A uniform partition of the time axis is defined at points $t_n = \vartheta - \delta t n$, where δt is the time step, and n successively takes integer values from 0 to some natural number $m = \vartheta/\delta t$. At each subinterval of time $[t_{n+1}, t_n]$, the search of the temperature T and flow velocity \mathbf{u} at $t = t_{n+1}$ consists of the following basic steps.

- Step 1. Given the temperature $T = T(t_n, \mathbf{x})$ at $t = t_n$ solve a set of linear algebraic equations derived from (8.11) and (8.12) with the appropriate boundary conditions in order to determine the velocity \mathbf{u} .
- Step 2. The ‘advective’ temperature $T_{adv} = T_{adv}(t_{n+1}, \mathbf{x})$ is determined by solving the advection heat equation backward in time, neglecting the diffusion term in Eq. (8.10). This can be done by replacing positive time steps by negative ones (see Section 8.4). Given the temperature $T = T_{adv}$ at $t = t_{n+1}$ steps 1 and 2 are then repeated to find the velocity $\mathbf{u}_{adv} = \mathbf{u}(t_{n+1}, \mathbf{x}; T_{adv})$.
- Step 3. The heat equation (8.10) is solved with appropriate boundary conditions and initial condition $\varphi_k(\mathbf{x}) = T_{adv}(t_{n+1}, \mathbf{x})$, $k = 0, 1, 2, \dots, m, \dots$ forward in time using velocity \mathbf{u}_{adv} in order to find $T(t_n, \mathbf{x}; \varphi_k)$.
- Step 4. The adjoint equation of (8.17) is then solved backward in time with appropriate boundary conditions and initial condition $\Psi(t_n, \mathbf{x}) = 2(T(t_n, \mathbf{x}; \varphi_k) - \chi(\mathbf{x}))$ using velocity \mathbf{u} in order to determine $\nabla J(\varphi_k) = \Psi(t_{n+1}, \mathbf{x}; \varphi_k)$.
- Step 5. The coefficient β_k is determined from (8.16), and the temperature is updated (i.e. φ_{k+1} is determined) from (8.15).

Steps 3 to 5 are repeated until

$$\delta\varphi_n = J(\varphi_n) + \|\nabla J(\varphi_n)\|^2 < \varepsilon, \quad (8.23)$$

where ε is a small constant. Temperature φ_k is then considered to be the approximation to the target value of the initial temperature $T(t_{n+1}, \mathbf{x})$. And finally, step 1 is used to determine the flow velocity $\mathbf{u}(t_{n+1}, \mathbf{x}; T(t_{n+1}, \mathbf{x}))$. Step 2 introduces a pre-conditioner to accelerate the convergence of temperature iterations in steps 3 to 5 at high Rayleigh number. At low Ra , step 2 is omitted and \mathbf{u}_{adv} is replaced by \mathbf{u} . After these algorithmic steps, we obtain temperature $T = T(t_n, \mathbf{x})$ and flow velocity $\mathbf{u} = \mathbf{u}(t_n, \mathbf{x})$ corresponding to $t = t_n$, $n = 0, \dots, m$. Based on the obtained results, we can use interpolation to reconstruct, when required, the entire process on the time interval $[0, \vartheta]$ in more detail.

Thus, at each subinterval of time we apply the VAR method to the heat equation only, iterate the direct and conjugate problems for the heat equation in order to find temperature, and determine backward flow from the Stokes and continuity equations twice (for ‘advective’ and ‘true’ temperatures). Compared to the VAR approach by Bunge *et al.* (2003), the described numerical approach is computationally less expensive, because we do not involve the Stokes equation in the iterations between the direct and conjugate problems (the numerical solution of the Stokes equation is the most time consuming calculation).

8.6 Application of the VAR method: restoration of mantle plume evolution

A plume is hot, narrow mantle upwelling that is invoked to explain hotspot volcanism. In a temperature-dependent viscosity fluid such as the mantle, a plume is characterised by a mushroom-shaped head and a thin tail. Upon impinging under a moving lithosphere, such a mantle upwelling should therefore produce a large amount of melt and successive massive eruption, followed by smaller but long-lived hot-spot activity fed from the plume tail (Morgan, 1972; Richards *et al.*, 1989; Sleep, 1990). Meanwhile, slowly rising plumes (a buoyancy flux of less than 10^3 kg s^{-1}) coming from the core–mantle boundary should have cooled so much that they would not melt beneath old lithosphere (Albers and Christensen, 1996).

Mantle plumes evolve in three distinguishing stages: (i) *immature*, i.e. an origin and initial rise of the plumes; (ii) *mature*, i.e. plume–lithosphere interaction, gravity spreading of plume head and development of overhangs beneath the bottom of the lithosphere, and partial melting of the plume material (see Ribe and Christensen, 1994; Moore *et al.*, 1998); and (iii) *overmature*, i.e. slowing-down of the plume rise and fading of the mantle plumes due to thermal diffusion (Davaille and Vatteville, 2005; Ismail-Zadeh *et al.*, 2006). The ascent and evolution of mantle plumes depend on the properties of the source region (that is, the thermal boundary layer) and the viscosity and thermal diffusivity of the ambient mantle. The properties of the source region determine the temperature and viscosity of the mantle plumes. Structure, flow rate and heat flux of the plumes are controlled by the properties of the mantle through which the plumes rise. While properties of the lower mantle (e.g. viscosity, thermal conductivity) are relatively constant during about 150 Myr lifetime of most plumes, source region properties can vary substantially with time as the thermal basal boundary layer feeding the plume is depleted of hot material (Schubert *et al.*, 2001). Complete local depletion of this boundary layer cuts the plume off from its source.

A mantle plume is a well-established structure in computer modelling and laboratory experiments. Numerical experiments on dynamics of mantle plumes (Trompert and Hansen, 1998a,b; Zhong, 2005) showed that the number of plumes increases and the rising plumes become thinner with an increase in Rayleigh number. Disconnected thermal plume structures appear in thermal convection at Ra greater than 10^7 (Hansen *et al.*, 1990; Malevsky *et al.*, 1992). At high Ra (in the hard turbulence regime) thermal plumes are torn off the boundary layer by the large-scale circulation or by non-linear interactions between plumes (Malevsky and Yuen, 1993). Plume tails can also be disconnected when the plumes are tilted by plate scale flow (see Olson and Singer, 1985; Steinberger and O’Connell, 1998). Ismail-Zadeh *et al.* (2006) presented an alternative explanation for the disconnected mantle plume heads and tails that is based on thermal diffusion of mantle plumes.

A dimensionless temperature-dependent viscosity law (Busse *et al.*, 1993) is employed in the models discussed in this chapter

$$\eta(T) = \exp\left(\frac{M}{T+G} - \frac{M}{0.5+G}\right), \quad (8.24)$$

where $M = [225/\ln(r)] - 0.25 \ln(r)$, $G = 15/\ln(r) - 0.5$, and r is the viscosity ratio between the upper and lower boundaries of the model domain. The temperature-dependent viscosity profile has its minimum at the core–mantle boundary. A more realistic viscosity profile (Forte and Mitrovica, 2001) will influence the evolution of mantle plumes, though it will not influence the restoration of the plumes.

The model domain is divided into $37 \times 37 \times 29$ rectangular finite elements to approximate the vector velocity potential by tricubic splines, and a uniform grid $112 \times 112 \times 88$ is employed for approximation of temperature, velocity and viscosity. Temperature in the heat equation (8.10) is approximated by finite differences and determined by the semi-Lagrangian method (see Section 7.8). A numerical solution to the Stokes and incompressibility equations (8.11) and (8.12) is based on the introduction of a two-component vector velocity potential and on the application of the Eulerian finite-element method with a tricubic-spline basis for computing the potential (Section 4.9 and 4.10). Such a procedure results in a set of linear algebraic equations with a symmetric positive-definite banded matrix. We solve the set of equations by the conjugate gradient method (Section 6.3.3).

8.6.1 Forward modelling

Here the evolution of mature mantle plumes is modelled initially forward in time. With $\alpha = 3 \times 10^{-5} \text{ K}^{-1}$, $\rho_{ref} = 4000 \text{ kg m}^{-3}$, $\Delta T = 3000 \text{ K}$, $h = 2800 \text{ km}$, $\eta_{ref} = 8 \times 10^{22} \text{ Pa s}$, and $\kappa = 10^{-6} \text{ m}^2 \text{ s}^{-1}$, the initial Rayleigh number is $Ra = 9.5 \times 10^5$. While plumes evolve in the convecting heterogeneous mantle, at the initial time it is assumed that the plumes develop in a laterally homogeneous temperature field, and hence the initial mantle temperature is considered to increase linearly with depth.

Mantle plumes are generated by random temperature perturbations at the top of the thermal source layer associated with the core–mantle boundary (Fig. 8.4a). The mantle material in the basal source layer flows horizontally toward the plumes. The reduced viscosity in this basal layer promotes the flow of the material to the plumes. Vertical upwelling of hot mantle material is concentrated in low viscosity conduits near the centrelines of the emerging plumes (Fig. 8.4b,c). The plumes move upward through the model domain, gradually forming structures with well-developed heads and tails. Colder material overlying the source layer (e.g. portions of lithospheric slabs subducted to the core–mantle boundary) replaces hot material at the locations where the source material is fed into mantle plumes. Some time is required to recover the volume of source material depleted due to plume feeding (Howard, 1966). Because the volume of upwelling material is comparable to the volume of the thermal source layer feeding the mantle plumes, hot material could eventually be exhausted, and mantle plumes would be starved thereafter.

The plumes diminish in size with time (Fig. 8.4d), and the plume tails disappear before the plume heads (Fig. 8.4e,f). We note that Fig. 8.4 presents a hot isothermal surface of the plumes. If colder isotherms are considered, the disappearance of the isotherms will occur later. But anyhow, hot or cold isotherms are plotted, plume tails will vanish before their heads. Results of recent laboratory experiments (Davaille and Vatteville, 2005) support

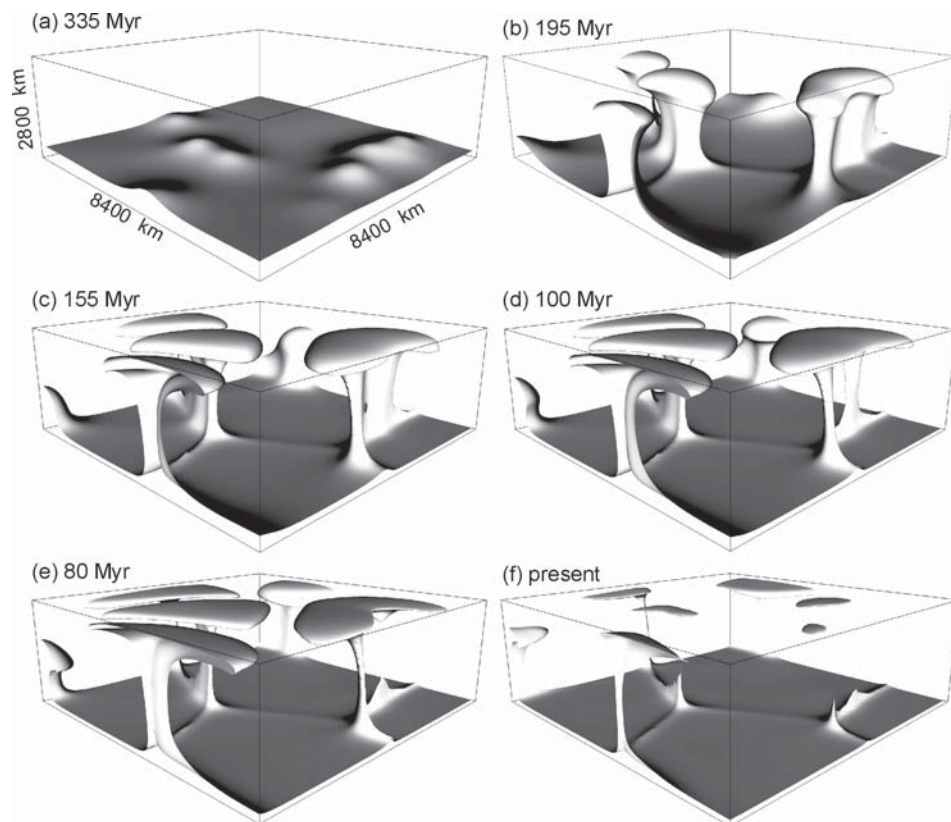


Fig. 8.4. Mantle plumes in the forward modelling at successive diffusion times: from 335 Myr ago (a) to the 'present' state of the plumes (f). The plumes are represented here and in Figs. 8.5 and 8.6 by isothermal surfaces at 3000 K. After Ismail-Zadeh *et al.* (2006).

strongly the numerical findings that plumes start disappearing from the bottom up and fade away by thermal diffusion.

At different stages in the plume decay one sees quite isolated plume heads, plume heads with short tails, and plumes with nearly pinched off tails. Different amounts of time are required for different mantle plumes to vanish into the ambient mantle, the required time depending on the geometry of the plume tails. Temperature loss is greater for sheet-like tails than for cylindrical tails. The tails of the cylindrical plumes (e.g. Fig. 8.4c, in the left part of the model domain) are still detectable after about 155 Myr. However, at this time the sheet-like tail of the large plume in the right part of the model domain (Fig. 8.4c) is already invisible and only its head is preserved in the uppermost mantle (Fig. 8.4f). Two-dimensional numerical experiments of steady-state convection (Leitch *et al.*, 1996) reveal a significant change in the centreline temperature of sheet-like plume tails compared with the cylindrical plume tail due to heat conduction in the horizontal direction.

The numerical results may have important implications for the interpretation of seismic tomographic images of mantle plumes. Finite-frequency seismic tomography images

(Montelli *et al.*, 2004) show that a number of plumes extend to mid-mantle depths but are not visible below these depths. From a seismological point of view, the absence of the plume tails could be explained as a combination of several factors (Romanowicz and Gung, 2002): elastic velocities are sensitive to composition as well as temperature; the effect of temperature on velocities decreases with increasing pressure (Karato, 1993); and wavefront healing effects make it difficult to accurately image low velocity bodies (Nolet and Dahlen, 2000). The ‘disappearance’ of the plume tails can hence be explained as the effects of poor tomographic resolution at deeper levels. Apart from this, the numerical results demonstrate the plausibility of finding a great diversity in the morphology of seismically imaged mantle plumes, including plume heads without tails and plumes with tails that are detached from their sources.

8.6.2 Backward modelling

To restore the prominent state of the plumes (Fig. 8.4d) in the past from their ‘present’ weak state (Fig. 8.4f), the VAR method can be employed. Figure 8.5 illustrates the restored states of the plumes (middle panel) and the temperature residuals δT (right panel) between the temperature $T(\mathbf{x})$ predicted by the forward model and the temperature $\tilde{T}(\mathbf{x})$ reconstructed to the same age:

$$\delta T(x_1, x_2) = \left[\int_0^h \left(T(x_1, x_2, x_3) - \tilde{T}(x_1, x_2, x_3) \right)^2 dx_3 \right]^{1/2}. \quad (8.25)$$

To study the effect of thermal diffusion on the restoration of mantle plumes, several experiments on mantle plume restoration were run for various Rayleigh number Ra (typically less than the initial Ra) and viscosity ratio r . Figure 8.6 presents the case of $r = 200$ and $Ra = 9.5 \times 10^3$ and shows several stages in the diffusive decay of the mantle plumes.

The dimensional temperature residuals are within a few degrees for the initial restoration period (Figs. 8.5i and 8.6h). The computations show that the errors (temperature residuals) get larger the farther the restorations move backward in time (e.g. $\delta T \approx 300$ K at the restoration time of more than 300 Myr, $r = 200$, and $Ra = 9.5 \times 10^3$). Compared with the case of $Ra = 9.5 \times 10^5$, one can see that the residuals become larger as the Rayleigh number decreases or thermal diffusion increases and viscosity ratio increases.

The quality of the restoration depends on the dimensionless Péclet number $Pe = hu_{\max}\kappa^{-1}$, where u_{\max} is the maximum flow velocity. According to the numerical experiments, the Péclet number corresponding to the temperature residual $\delta T = 600$ K is $Pe = 10$; Pe should not be less than about 10 for a high quality plume restoration.

8.6.3 Performance of the numerical algorithm

Here we analyse the performance of the VAR data assimilation algorithm for various Ra and r . The performance of the algorithm is evaluated in terms of the number of iterations

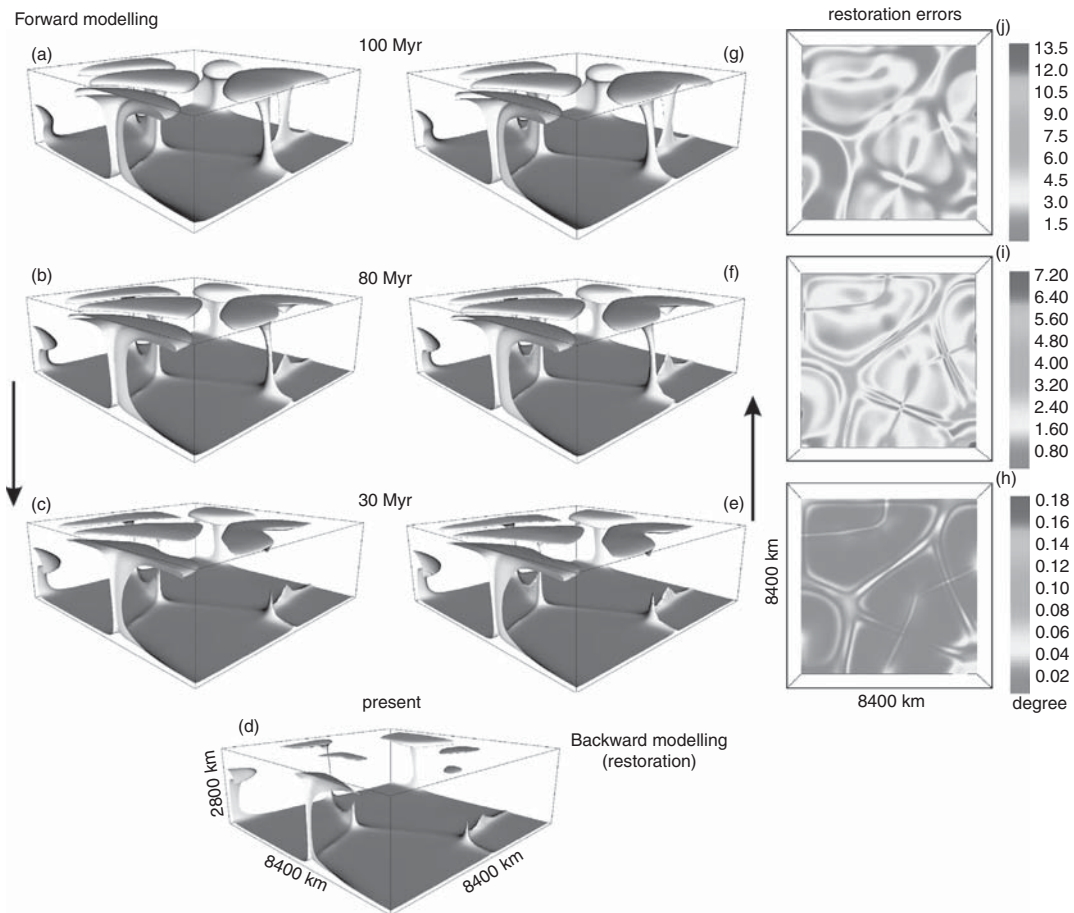


Fig. 8.5. Mantle plume diffusion ($r = 20$ and $Ra = 9.5 \times 10^5$) in the forward modelling at successive diffusion times: from 100 Myr ago to the 'present' state of the plumes (left panel, a–d). Restored mantle plumes in the backward modelling (central panel, e–g) and restoration errors (right panel, h–j). After Ismail-Zadeh *et al.* (2006). (In colour as Plate 3. See colour plates section.)

n required to achieve a prescribed relative reduction of $\delta\varphi_n$ (inequality (8.23)). Figure 8.7 presents the evolution of the objective functional $J(\varphi_n)$ and the norm of the gradient of the objective functional $\|\nabla J(\varphi_n)\|$ versus the number of iterations at time about 0.5θ . For other time steps we observe a similar evolution of J and $\|\nabla J\|$.

Both the objective functional and the norm of its gradient show a quite rapid decrease after about seven iterations for $Ra = 9.5 \times 10^5$ and $r = 20$ (curves 1). The same rapid convergence as a function of adjoint iterations is observed in the Bunge *et al.* (2003) case. As Ra decreases and thermal diffusion increases (curves 2–4) the performance of the algorithm becomes poor: more iterations are needed to achieve the prescribed ε . All curves illustrate that the first four to seven iterations contribute mainly to the reduction of $\delta\varphi_n$. The convergence drops after a relatively small number of iterations. The curves approach the horizontal line with an increase in the number of iterations, because β_k tends to zero with a large number of iterations (see Eq. (8.6)). The increase of $\|\nabla J\|$ at $k = 2$ is associated with uncertainty of this gradient at $k = 1$.

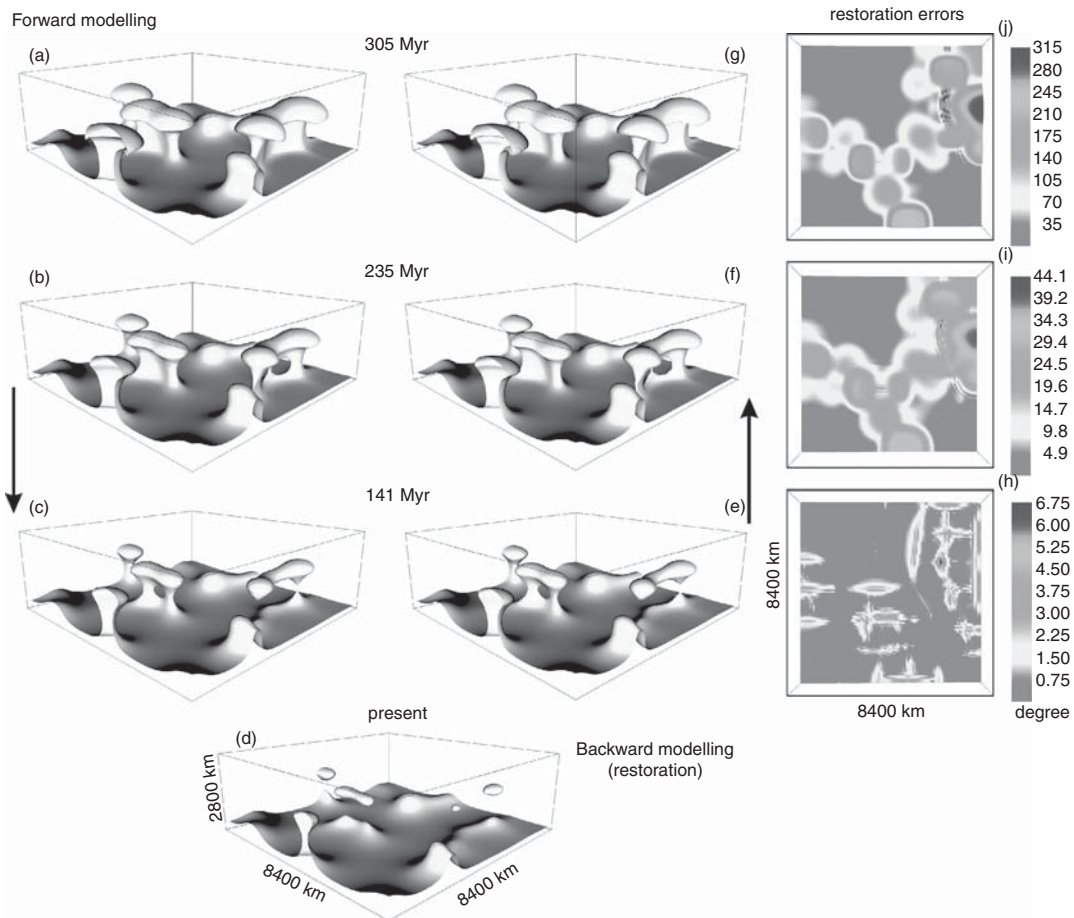


Fig. 8.6. Mantle plume diffusion ($r = 200$ and $Ra = 9.5 \times 10^3$) in the forward modelling at successive diffusion times: from 305 Myr ago to the 'present' state of the plumes (left panel, a-d). Restored mantle plumes in the backward modelling (central panel, e-g) and restoration errors (right panel, h-j). After Ismail-Zadeh *et al.* (2006). (In colour as Plate 4. See colour plates section.)

Implementation of minimisation algorithms requires the evaluation of both the objective functional and its gradient. Each evaluation of the objective functional requires an integration of the model equation (8.10) with the appropriate boundary and initial conditions, whereas the gradient is obtained through the backward integration of the adjoint equations (8.17). The performance analysis shows that the CPU time required to evaluate the gradient J is about the CPU time required to evaluate the objective functional itself, and this is because the direct and adjoint heat problems are described by the same equations.

Despite its simplicity, the minimisation algorithm used in this study provides for a rapid convergence and good quality of optimisation at high Rayleigh numbers (low thermal diffusion). The convergence rate and the quality of optimisation become worse with the decreasing Rayleigh number. The use of the limited-memory quasi-Newton algorithm L-BFGS (Liu and Nocedal, 1989) might provide for a better convergence rate and quality of optimisation (Zou *et al.*, 1993). Meanwhile, we note that although an improvement of the convergence rate by using another minimisation algorithm (e.g. L-BFGS) will reduce

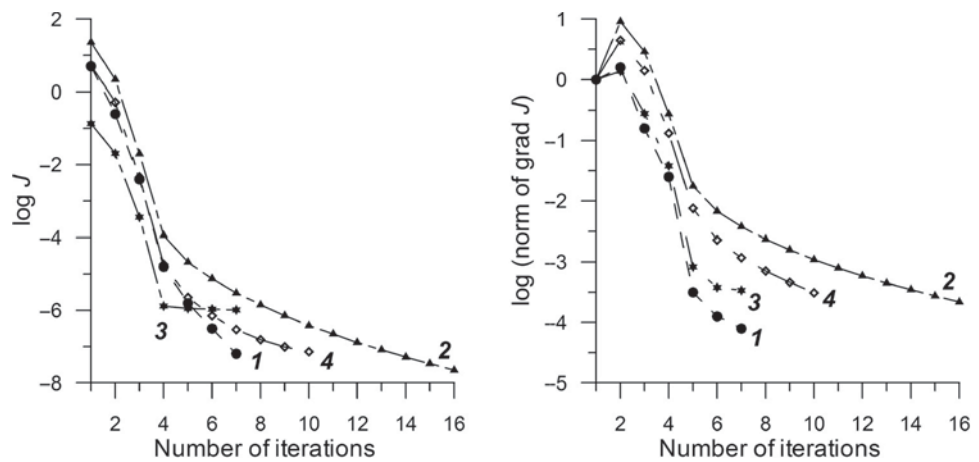


Fig. 8.7. Relative reductions of the objective functional J (left panel) and the norm of the gradient of J (right panel) as functions of the number of iterations. Curves: 1, $r = 20$, $Ra = 9.5 \times 10^5$; 2, $r = 20$, $Ra = 9.5 \times 10^2$; 3, $r = 200$, $Ra = 9.5 \times 10^3$; 4, $r = 200$, $Ra = 9.5 \times 10^2$. After Ismail-Zadeh *et al.* (2006).

the computational expense associated with the solving of the problem under question, this reduction would be not significant, because the large portion (about 70%) of the computer time is spent to solve the 3-D Stokes equations.

8.7 Challenges in VAR data assimilation

Although the VAR data assimilation technique described above can theoretically be applied to many problems of mantle and lithosphere dynamics, practical implementation of the technique for modelling of real geodynamic processes backward in time (to restore the temperature and flow pattern in the past) is not a simple task. The mathematical model of mantle dynamics described by a set of equations (8.10)–(8.12) is simple, and many complications are omitted. A viscosity increase from the upper to the lower mantle is not included in the model, although it is suggested by studies of the geoid (Ricard *et al.*, 1993), post-glacial rebound (Mitrovica, 1996), and joint inversion of convection and glacial isostatic adjustment data (Mitrovica and Forte, 2004). The adiabatic heating/cooling term in the heat equation can provide more realistic distribution of temperature in the mantle, especially near the thermal boundary layer. The numerical models presented in Section 8.6 do not include phase transformations (Liu *et al.*, 1991; Honda *et al.*, 1993a,b; Harder and Christensen, 1996), although the phase changes can influence the evolution of mantle plumes retarding/accelerating their ascent. The coefficient of thermal expansion (see Chopelas and Boehler, 1989; Hansen *et al.*, 1991; 1993) and the coefficient of thermal conductivity (Hofmeister, 1999) are not constant in the mantle and vary with depth and temperature. Moreover, if the findings of Badro *et al.* (2004) of a significant increase in the radiative

thermal conductivity at high pressure are relevant to the lower mantle, plume tails should diffuse away even faster than the studied models predict. To consider these complications in the VAR data assimilation, the adjoint equations should be derived each time when the set of the equations is changed. The cost to be paid is in software development since an adjoint model has to be developed.

8.7.1 Smoothness of observational data

The solution $T(\vartheta, \cdot; \varphi)$ of the heat equation (8.10) with appropriate boundary and initial conditions is a sufficiently smooth function and belongs to space $L_2(\Omega)$. The present temperature χ_δ derived from the seismic tomography is a representation of the exact temperature χ of the Earth and so it must also belong to this space and hence be rather smooth; otherwise, the objective functional J cannot be defined. Therefore, before any assimilation of the present temperature data can be attempted, the data must be smoothed. The smoothing of the present temperature improves the convergence of the iterations.

8.7.2 Smoothness of the target temperature

If mantle temperature in the geological past was not a smooth function of space variables, recovery of this temperature by using the VAR method is not effective because the iterations converge very slowly to the target temperature. Here we explain the problem of recovering the initial temperature on the basis of three one-dimensional model tasks: restoration of a smooth, piece-wise smooth and discontinuous target function. We note that the temperature in the Earth's mantle is not a discontinuous function but its shape can be close to a step function.

The dynamics of a physical system is assumed to be described by the Burgers equation $u_t + uu_x = u_{xx}$, $0 \leq t \leq 1$, $0 \leq x \leq 2\pi$ with the boundary conditions $u(t, 0) = 0$, $u(t, 2\pi) = 0$, $0 \leq t \leq 1$ and the condition $u_\theta = u(1, x; u_0)$, $0 \leq x \leq 2\pi$ at $t = 1$, where the variable u can denote temperature. The problem is to recover the function $u_0 = u_0(x)$, $0 \leq x \leq 2\pi$ at $t = 0$ (the state in the past) from the function $u_\theta = u_\theta(x)$, $0 \leq x \leq 2\pi$ at $t = 1$ (its present state). The finite difference approximations and the variational method are applied to the Burgers equation with the appropriate boundary and initial conditions.

Task 1. Consider the sufficiently smooth function $u_0 = \sin(x)$, $0 \leq x \leq 2\pi$. The functions u_0 and u_θ are shown in Fig. 8.8a. Figures 8.8b and c illustrate the iterations φ_k using the iterative scheme similar to Eq. (8.15) for $k = 0, 4, 6$ and the residual $r_6(x) = u_0(x) - \varphi_6(x)$, $0 \leq x \leq 2\pi$ respectively. We see that iterations converge rather rapid for the sufficiently smooth target function.

Task 2. Now consider the continuous piece-wise smooth function $u_0 = 3x/(2\pi)$, $0 \leq x \leq 2\pi/3$ and $u_0 = 3/2 - 3x/(2\pi)$, $2\pi/3 \leq x \leq 2\pi$. Figure 8.8 presents (d) the functions u_0 and u_θ , (e) the successive approximations φ_k for $k = 0, 4, 1000$, and (f) the residual $r_{1000}(x) = u_0(x) - \varphi_{1000}(x)$, $0 \leq x \leq 2\pi$, respectively. This example shows that a large number of iterations is required to reach the target function.

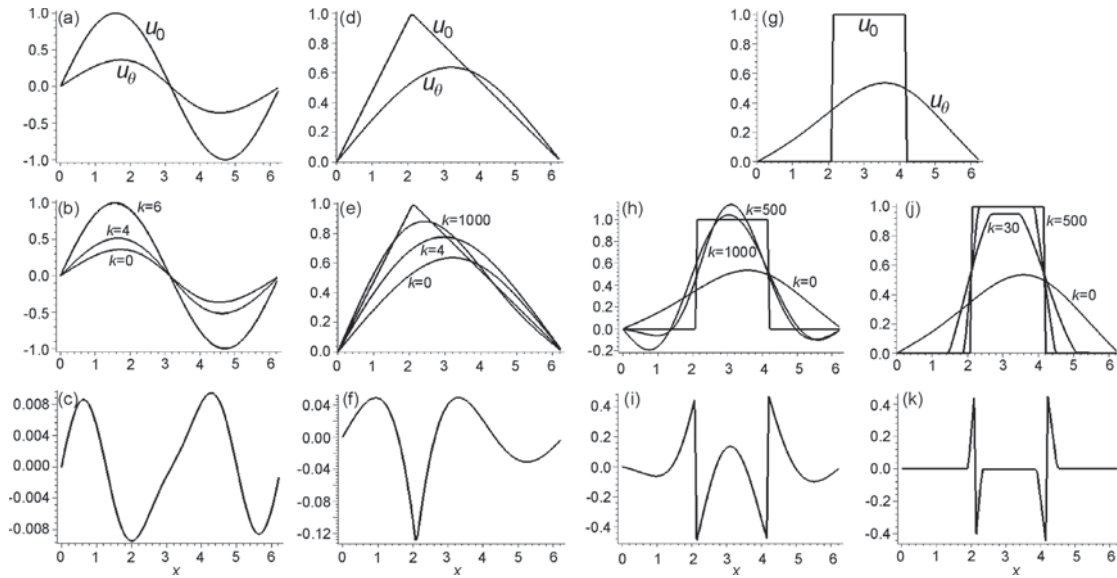


Fig. 8.8. Recovering function u_0 from the smooth guess function u_θ . The sufficiently smooth u_0 (a–c); continuous piece-wise smooth function u_0 (d–f); and discontinuous function u_0 (g–k). Plots of u_0 and u_θ are presented at (a), (d) and (g); successive approximations to u_0 at (b), (e), (h) and (j); and the residual functions at (c), (f), (i) and (k). After Ismail-Zadeh *et al.* (2006).

Task 3. Consider the discontinuous function u_0 , which takes 1 at $2\pi/3 \leq x \leq 4\pi/3$ and 0 in other points of the closed interval $0 \leq x \leq 2\pi$. Figure 8.8 presents (g) the functions u_0 and u_θ , (h) the successive approximations φ_k for $k = 0, 500, 1000$, and (e) the residual $r_{1000}(x) = u_0(x) - \varphi_{1000}(x)$, $0 \leq x \leq 2\pi$, respectively. We see that convergence to the target temperature is very poor.

To improve the convergence to the target function, a modification of the variational method based on *a priori* information about a desired solution can be used (Korotkii and Tsepelev, 2003). Figure 8.8 (j) shows the successive approximations $\tilde{\varphi}_k$ for $k = 0, 30, 500$, and (k) the residual $\tilde{r}_{500}(x) = u_0(x) - \tilde{\varphi}_{500}(x)$, $0 \leq x \leq 2\pi$, respectively. The approximations $\tilde{\varphi}_k$ based on the method of gradient projection (Vasiliev, 2002) converge to the target solution better than approximations generated by Eq. (8.5).

8.7.3 Numerical noise

If the initial temperature guess φ_0 is a smooth function, all successive temperature iterations φ_k in scheme (8.15) should be smooth functions too, because the gradient of the objective functional ∇J is a smooth function since it is the solution to the adjoint problem (8.17). However, the temperature iterations φ_k are polluted by small perturbations (errors), which are inherent in any numerical experiment (Section 8.12). These perturbations can grow with time. Samarskii *et al.* (1997) applied a VAR method to a 1-D backward heat diffusion problem and showed that the solution to this problem becomes noisy if the initial temperature guess is slightly perturbed, and the amplitude of this noise increases with the initial perturbations of the temperature guess. To reduce the noise they used a special filter and

illustrated the efficiency of the filter. This filter is based on the replacement of iterations (8.15) by the following iterative scheme:

$$\mathbf{B}(\varphi_{k+1} - \varphi_k) = -\beta_k \nabla J(\varphi_k), \quad (8.26)$$

where $\mathbf{B}y = y - \nabla^2 y$. Unfortunately, employment of this filter increases the number of iterations to obtain the target temperature and it becomes quite expensive computationally, especially when the model is three-dimensional. Another way to reduce the noise is to employ high-order adjoint (Alekseev and Navon, 2001) or regularisation (Tikhonov, 1963; Lattes and Lions, 1969; Samarskii and Vabischevich, 2004) techniques.

8.8 Quasi-reversibility (QRV) method

The principal idea of the quasi-reversibility (QRV) method is based on the transformation of an ill-posed problem into a well-posed problem (Lattes and Lions, 1969). In the case of the backward heat equation, this implies an introduction of an additional term into the equation, which involves the product of a small regularisation parameter and higher-order temperature derivative. The additional term should be sufficiently small compared to other terms of the heat equation and allow for simple additional boundary conditions. The data assimilation in this case is based on a search of the best fit between the forecast model state and the observations by minimising the regularisation parameter. The QRV method is proven to be well suited for smooth and non-smooth input data (Lattes and Lions, 1969; Samarskii and Vabischevich, 2004).

To explain the transformation of the problem, we follow Ismail-Zadeh *et al.* (2007) and consider the following boundary-value problem for the one-dimensional heat conduction problem

$$\frac{\partial T(t, x)}{\partial t} = \frac{\partial^2 T(t, x)}{\partial x^2}, \quad 0 \leq x \leq \pi, \quad 0 \leq t \leq t^*, \quad (8.27)$$

$$T(t, x = 0) = T(t, x = \pi) = 0, \quad 0 \leq t \leq t^*, \quad (8.28)$$

$$T(t = 0, x) = \frac{1}{4n + 1} \sin((4n + 1)x), \quad 0 \leq x \leq \pi. \quad (8.29)$$

The analytical solution to (8.27)–(8.29) can be obtained in the following form

$$T(t, x) = \frac{1}{4n + 1} \exp(-(4n + 1)^2 t) \sin((4n + 1)x). \quad (8.30)$$

Figure 8.9 presents the solution (solid curves) for time interval $0 \leq t \leq t^* = 0.14$ and $n = 1$.

It is known that the backward heat conduction problem is ill-posed (e.g. Kirsch, 1996). To transform the problem into a well-posed problem, we introduce a term in Eq. (8.27) involving

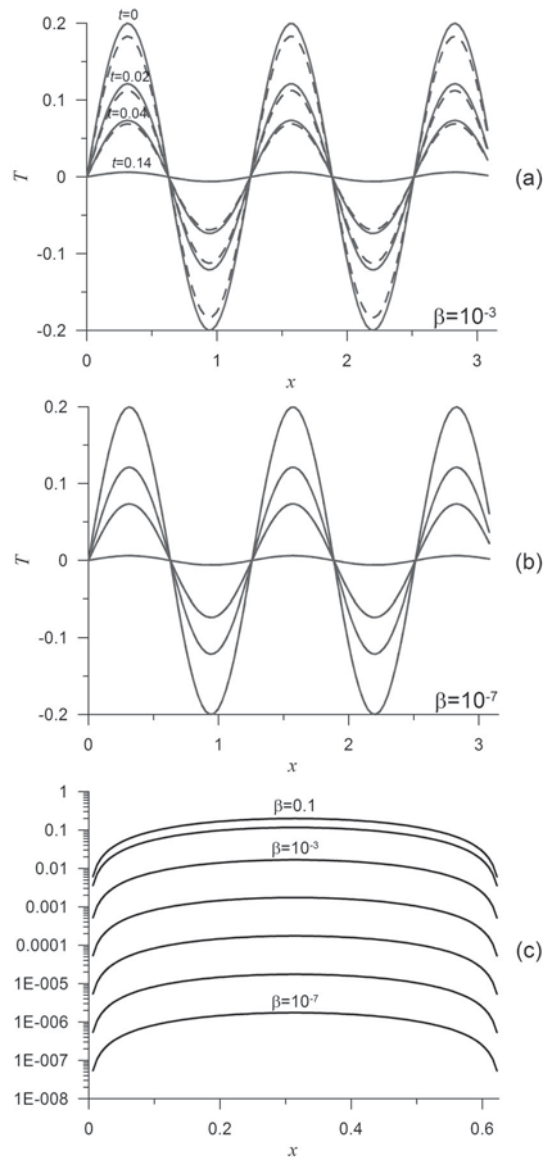


Fig. 8.9. Comparison of the exact solutions to the heat conduction problem (red solid curves; a and b) and to the regularised backward heat conduction problem (a: $\beta = 10^{-3}$ and b: $\beta = 10^{-7}$; blue dashed curves). The temperature residual between two solutions is presented in panel c at various values of the regularisation parameter β . After Ismail-Zadeh *et al.* (2007). (In colour as Plate 5. See colour plates section.)

the product of a small parameter $\beta > 0$ and the higher-order temperature derivative:

$$\frac{\partial T_{\beta}(t, x)}{\partial t} = \frac{\partial^2 T_{\beta}(t, x)}{\partial x^2} - \beta \frac{\partial^4}{\partial x^4} \left(\frac{\partial T_{\beta}(t, x)}{\partial t} \right), \quad 0 \leq x \leq \pi, \quad 0 \leq t \leq t^*, \quad (8.31)$$

$$T_\beta(t, x = 0) = T_\beta(t, x = \pi) = 0, \quad 0 \leq t \leq t^*, \quad (8.32)$$

$$\frac{\partial^2 T_\beta(t, x = 0)}{\partial x^2} = \frac{\partial^2 T_\beta(t, x = \pi)}{\partial x^2} = 0, \quad 0 \leq t \leq t^*, \quad (8.33)$$

$$T_\beta(t = t^*, x) = \frac{1}{4n + 1} \exp(-(4n + 1)^2 t^*) \sin((4n + 1)x), \quad 0 \leq x \leq \pi. \quad (8.34)$$

Here the initial condition is assumed to be the solution (8.30) to the heat conduction problem (8.27)–(8.29) at $t = t^*$. The subscript β at T_β is used to emphasise the dependence of the solution to problem (8.31)–(8.34) on the regularisation parameter. The analytical solution to the regularised backward heat conduction problem (8.31)–(8.34) is represented as:

$$T_\beta(t, x) = A_n \exp\left(\frac{-(4n + 1)^2 t}{1 + \beta(4n + 1)^4}\right) \sin((4n + 1)x),$$

$$A_n = \frac{1}{4n + 1} \exp(-(4n + 1)^2 t^*) \exp^{-1}\left(\frac{-(4n + 1)^2 t^*}{1 + \beta(4n + 1)^4}\right), \quad (8.35)$$

and the solution approaches the initial condition for the problem (8.27)–(8.29) at $t = 0$ and $\beta \rightarrow 0$. Figure 8.9a,b illustrates the solution to the regularised problem at two values of β (dashed curves) and $n = 1$. The temperature residual (Fig. 8.9c) indicates that the solution (8.35) approaches the solution (8.30) with $\beta \rightarrow 0$.

Samarskii and Vabischevich (2004) estimated the stability of the solution to problem (8.31)–(8.33) with respect to the initial condition expressed in the form $T_\beta(t = t^*, x) = T_\beta^*$:

$$\|T_\beta(t, x)\| + \beta \|\partial T_\beta(t, x)/\partial x\| \leq C \left(\|T_\beta^*\| + \beta \|\partial T_\beta^*/\partial x\| \right) \exp\left[(t^* - t)\beta^{-1/2}\right],$$

where C is a constant, and showed that the natural logarithm of errors will increase in direct proportion to time and inversely to the root square of the regularisation parameter.

Any regularisation has its advantages and disadvantages. A regularising operator is used in a mathematical problem to (i) accelerate a convergence; (ii) fulfil the physical laws (e.g. maximum principal, conservation of energy, etc.) in discrete equations; (iii) suppress a noise in input data and in numerical computations; and (iv) take into account *a priori* information about an unknown solution and hence to improve a quality of computations. The major drawback of regularisation is that the accuracy of the solution to a regularised problem is always lower than that to a non-regularised problem.

We should mention that the transformation to the regularised backward heat problem is not only a mathematical approach to solving ill-posed backward heat problems, but has some physical meaning: it can be explained on the basis of the concept of relaxing heat flux for heat conduction (Vernotte, 1958). The classical Fourier heat conduction theory provides the infinite velocity of heat propagation in a region. The instantaneous heat propagation is unrealistic, because the heat is a result of the vibration of atoms and the vibration propagates in a finite speed (Morse and Feshbach, 1953). To accommodate the finite velocity of heat propagation, a modified heat flux model was proposed by Vernotte (1958) and Cattaneo (1958).

The modified Fourier constitutive equation (sometimes called the Riemann law of heat conduction) is expressed as $\vec{Q} = -k\nabla T - \tau \partial \vec{Q}/\partial t$, where \vec{Q} is the heat flux, and k is the

coefficient of thermal conductivity. The thermal relaxation time $\tau = k / (\rho c_p v^2)$ is usually recognised to be a small parameter (Yu *et al.*, 2004), where ρ is the density, c_p is the specific heat, and v is the heat propagation velocity. The situation for $\tau \rightarrow 0$ leads to instantaneous diffusion at infinite propagation speed, which coincides with the classical thermal diffusion theory. The heat conduction equation $\partial T / \partial t = \nabla^2 T + \tau \partial^2 T / \partial t^2$ based on non-Fourier heat flux can be considered as a regularised heat equation. If the Fourier law is modified further by an addition of the second derivative of heat flux, e.g. $\vec{Q} = -k \nabla T + \beta \frac{\partial^2 \vec{Q}}{\partial t^2}$, where small β is the relaxation parameter of heat flux (Bubnov, 1976, 1981), the heat conduction equation can be transformed into a higher-order regularised heat equation similar to Eq. (8.31).

8.8.1 The QRV method for restoration of thermo-convective flow

For convenience, we present a set of equations (8.10)–(8.12) with the relevant boundary and initial conditions as two mathematical problems. Namely, we consider the *boundary-value problem for the flow velocity* (it includes the Stokes equation, the incompressibility equation subject to appropriate boundary conditions)

$$\nabla P = \text{div}(\eta(T)\mathbf{E}) + RaT\mathbf{e}, \quad \mathbf{x} \in \Omega, \quad (8.36)$$

$$\text{div} \mathbf{u} = 0, \quad \mathbf{x} \in \Omega, \quad (8.37)$$

$$\mathbf{u} \cdot \mathbf{n} = 0, \quad \partial \mathbf{u}_\tau / \partial \mathbf{n} = 0, \quad \mathbf{x} \in \partial \Omega, \quad (8.38)$$

where \mathbf{u}_τ is the projection of the velocity vector onto the tangent plane at the same point on the model boundary, and *the initial-boundary-value problem for temperature* (it includes the heat equation subject to appropriate boundary and initial conditions)

$$\partial T / \partial t + \mathbf{u} \cdot \nabla T = \nabla^2 T + f, \quad t \in [0, \vartheta], \quad \mathbf{x} \in \Omega, \quad (8.39)$$

$$\sigma_1 T + \sigma_2 \partial T / \partial \mathbf{n} = T_*, \quad t \in [0, \vartheta], \quad \mathbf{x} \in \partial \Omega, \quad (8.40)$$

$$T(0, \mathbf{x}) = T_0(\mathbf{x}), \quad \mathbf{x} \in \Omega, \quad (8.41)$$

where T_* is the given temperature.

The direct problem of thermo-convective flow can be formulated as follows: find the velocity $\mathbf{u} = \mathbf{u}(t, \mathbf{x})$, the pressure $P = P(t, \mathbf{x})$, and the temperature $T = T(t, \mathbf{x})$ satisfying boundary value problem (8.36)–(8.38) and initial-boundary-value problem (8.39)–(8.41). We can formulate the inverse problem in this case as follows: find the velocity, pressure, and temperature satisfying boundary-value problem (8.36)–(8.38) and the final-boundary value problem that includes Eqs. (8.39) and (8.40) and the final condition:

$$T(\vartheta, \mathbf{x}) = T_\vartheta(\mathbf{x}), \quad \mathbf{x} \in \Omega, \quad (8.42)$$

where T_ϑ is the temperature at time $t = \vartheta$.

To solve the inverse problem by the QRV method, Ismail-Zadeh *et al.* (2007) considered the following regularised backward heat problem to define temperature in the past from the

known temperature $T_\vartheta(\mathbf{x})$ at present time $t = \vartheta$:

$$\partial T_\beta / \partial t - \mathbf{u}_\beta \cdot \nabla T_\beta = \nabla^2 T_\beta + f - \beta \Lambda(\partial T_\beta / \partial t), \quad t \in [0, \vartheta], \quad \mathbf{x} \in \Omega, \quad (8.43)$$

$$\sigma_1 T_\beta + \sigma_2 \partial T_\beta / \partial \mathbf{n} = T_*, \quad t \in (0, \vartheta), \quad \mathbf{x} \in \partial \Omega, \quad (8.44)$$

$$\sigma_1 \partial^2 T_\beta / \partial \mathbf{n}^2 + \sigma_2 \partial^3 T_\beta / \partial \mathbf{n}^3 = 0, \quad t \in (0, \vartheta), \quad \mathbf{x} \in \partial \Omega, \quad (8.45)$$

$$T_\beta(\vartheta, \mathbf{x}) = T_\vartheta(\mathbf{x}), \quad \mathbf{x} \in \Omega, \quad (8.46)$$

where $\Lambda(T) = \partial^4 T / \partial x_1^4 + \partial^4 T / \partial x_2^4 + \partial^4 T / \partial x_3^4$, and the boundary value problem to determine the fluid flow:

$$\nabla P_\beta = -\text{div} [\eta(T_\beta) \mathbf{E}(\mathbf{u}_\beta)] + Ra T_\beta \mathbf{e}, \quad \mathbf{x} \in \Omega, \quad (8.47)$$

$$\text{div} \mathbf{u}_\beta = 0, \quad \mathbf{x} \in \Omega, \quad (8.48)$$

$$\mathbf{u}_\beta \cdot \mathbf{n} = 0 \text{ (and/or } \partial(\mathbf{u}_\beta)_\tau / \partial \mathbf{n} = 0), \quad \mathbf{x} \in \partial \Omega, \quad (8.49)$$

where the sign of the velocity field is changed (\mathbf{u}_β by $-\mathbf{u}_\beta$) in Eqs. (8.43) and (8.47) to simplify the application of the total variation diminishing (TVD) method (see Section 7.9) for solving (8.43)–(8.46). Hereinafter we refer to temperature T_β as the input temperature for the problem (8.43)–(8.49). The core of the transformation of the heat equation is the addition of a high-order differential expression $\Lambda(\partial T_\beta / \partial t)$ multiplied by a small parameter $\beta > 0$. Note that Eq. (8.45) is added to the boundary conditions to properly define the regularised backward heat problem. The solution to the regularised backward heat problem is stable for $\beta > 0$, and the approximate solution to (8.43)–(8.49) converges to the solution of (8.36)–(8.40), and (8.42) in some spaces, where the conditions of well-posedness are met (Samarskii and Vabischevich, 2004). Thus, the inverse problem of thermo-convective mantle flow is reduced to determination of the velocity $\mathbf{u}_\beta = \mathbf{u}_\beta(t, \mathbf{x})$, the pressure $P_\beta = P_\beta(t, \mathbf{x})$, and the temperature $T_\beta = T_\beta(t, \mathbf{x})$ satisfying (8.43)–(8.49).

8.8.2 Optimisation problem

A maximum of the following functional is sought with respect to the regularisation parameter β :

$$\delta - \|T(t = \vartheta, \cdot; T_{\beta_k}(t = 0, \cdot)) - \varphi(\cdot)\| \rightarrow \max_k, \quad (8.50)$$

$$\beta_k = \beta_0 q^{k-1}, \quad k = 1, 2, \dots, \aleph, \quad (8.51)$$

where sign $\| \cdot \|$ denotes the norm in the space $L_2(\Omega)$. Since in what follows the dependence of solutions on initial temperature data is important, we introduce these data explicitly into the mathematical representation of temperature. Here $T_k = T_{\beta_k}(t = 0, \cdot)$ is the solution to the regularised backward heat problem (8.43)–(8.45) at $t = 0$; $T(t = \vartheta, \cdot; T_k)$ is the solution to the heat problem (8.39)–(8.41) at the initial condition $T(t = 0, \cdot) = T_k$ at time $t = \vartheta$; φ is the known temperature at $t = \vartheta$ (the input data on the present temperature);

small parameters $\beta_0 > 0$ and $0 < q < 1$ are defined below; and $\delta > 0$ is a given accuracy. When q tends to unity, the computational cost becomes large; and when q tends to zero, the optimal solution can be missed.

The prescribed accuracy δ is composed from the accuracy of the initial data and the accuracy of computations. When the input noise decreases and the accuracy of computations increases, the regularisation parameter is expected to decrease. However, estimates of the initial data errors are usually inaccurate. Estimates of the computation accuracy are not always known, and when they are available, the estimates are coarse. In practical computations, it is more convenient to minimise the following functional with respect to (8.51)

$$\|T_{\beta_{k+1}}(t=0, \cdot) - T_{\beta_k}(t=0, \cdot)\| \rightarrow \min_k, \quad (8.52)$$

where misfit between temperatures obtained at two adjacent iterations must be compared. To implement the minimisation of temperature residual (8.50), the inverse problem (8.43)–(8.49) must be solved on the entire time interval as well as the direct problem (8.36)–(8.41) on the same time interval. This at least doubles the amount of computations. The minimisation of functional (8.52) has a lower computational cost, but it does not rely on *a priori* information.

8.8.3 Numerical algorithm for QRV data assimilation

In this section we describe the numerical algorithm for solving the inverse problem of thermo-convective mantle flow using the QRV method. We consider a uniform temporal partition $t_n = \vartheta - \delta t n$ (as defined in Section 8.5) and prescribe some values to parameters β_0 , q and \mathfrak{N} (e.g. $\beta_0 = 10^{-3}$, $q = 0.1$ and $\mathfrak{N} = 10$). According to (8.51) a sequence of the values of the regularisation parameter $\{\beta_k\}$ is defined. For each value $\beta = \beta_k$ model temperature and velocity are determined in the following way.

- Step 1. Given the temperature $T_\beta = T_\beta(t, \cdot)$ at $t = t_n$, the velocity $\mathbf{u}_\beta = \mathbf{u}_\beta(t_n, \cdot)$ is found by solving problem (8.47)–(8.49). This velocity is assumed to be constant on the time interval $[t_{n+1}, t_n]$.
- Step 2. Given the velocity $\mathbf{u}_\beta = \mathbf{u}_\beta(t_n, \cdot)$, the new temperature $T_\beta = T_\beta(t, \cdot)$ at $t = t_{n+1}$ is found on the time interval $[t_{n+1}, t_n]$ subject to the final condition $T_\beta = T_\beta(t_n, \cdot)$ by solving the regularised problem (8.43)–(8.46) backward in time.
- Step 3. Upon the completion of steps 1 and 2 for all $n = 0, 1, \dots, m$, the temperature $T_\beta = T_\beta(t_n, \cdot)$ and the velocity $\mathbf{u}_\beta = \mathbf{u}_\beta(t_n, \cdot)$ are obtained at each $t = t_n$. Based on the computed solution we can find the temperature and flow velocity at each point of time interval $[0, \vartheta]$ using interpolation.
- Step 4a. The direct problem (8.39)–(8.41) is solved assuming that the initial temperature is given as $T_\beta = T_\beta(t=0, \cdot)$, and the temperature residual (8.50) is found. If the residual does not exceed the predefined accuracy, the calculations are terminated, and the results obtained at step 3 are considered as the final ones. Otherwise,

parameters β_0 , q and \mathfrak{N} entering Eq. (8.51) are modified, and the calculations are continued from step 1 for new set $\{\beta_k\}$.

- Step 4b. The functional (8.52) is calculated. If the residual between the solutions obtained for two adjacent regularisation parameters satisfies a predefined criterion (the criterion should be defined by a user, because no *a priori* data are used at this step), the calculation is terminated, and the results obtained at step 3 are considered as the final ones. Otherwise, parameters β_0 , q and \mathfrak{N} entering Eq. (8.51) are modified, and the calculations are continued from step 1 for new set $\{\beta_k\}$.

In a particular implementation, either step 4a or step 4b is used to terminate the computation. This algorithm allows (i) organising a certain number of independent computational modules for various values of the regularised parameter β_k that find the solution to the regularised problem using steps 1–3 and (ii) determining *a posteriori* an acceptable result according to step 4a or step 4b.

8.9 Application of the QRV method: mantle plume evolution

To compare the numerical results obtained by the QRV method with that obtained by the VAR and BAD methods described in this chapter, we develop the same forward model for mantle plume evolution as presented in Section 8.6. Figure 8.10 (panels a–d) illustrates the evolution of mantle plumes in the forward model. The state of the plumes at the ‘present’ time (Fig. 8.10d) obtained by solving the direct problem was used as the input temperature for the inverse problem (an assimilation of the ‘present’ temperature to the past). Note that this initial state (input temperature) is given with an error introduced by the numerical algorithm used to solve the direct problem. Figure 8.10 illustrates the states of the plumes restored by the QRV method (panels e–g) and the residual δT (see Eq. (8.26) and panel h) between the initial temperature for the forward model (Fig. 8.10a) and the temperature $\tilde{T}(\mathbf{x})$ assimilated to the same age (Fig. 8.10g). To check the stability of the algorithm, a forward model of the restored plumes is computed using the solution to the inverse problem at the time of 265 Myr ago (Fig. 8.10g) as the initial state for the forward model. The result of this run is shown in Fig. 8.10i.

To compare the accuracy of the data assimilation methods, a restoration model from the ‘present’ time (Fig. 8.10d) to the time of 265 Myr ago was developed using the BAD method. Figure 8.10 shows the BAD model results (panels e1–g1) together with the temperature residual (panel h1) between the initial temperature (panel a) and the temperature assimilated to the same age (panel g1). The VAR method was not used to assimilate data within the time interval of more than 100 Myr (for $Ra \approx 10^6$), because proper filtering of the increasing noise is required to smooth the input data and solution (Section 8.7).

Figure 8.11a presents the residual $J_1(\beta) = \|T_0(\cdot) - T_\beta(t = t_0, \cdot; T_\vartheta)\|$ between the initial temperature T_0 at $t_0 = 265$ Myr ago and the restored temperature (to the same time) obtained by solving the inverse problem with the input temperature T_ϑ . The optimal accuracy is attained at $\beta^* = \arg \min\{J_1(\beta) : \beta = \beta_k, k = 1, 2, \dots, 10\} \approx 10^{-7}$ in the case of $r = 20$, and at $\beta^* \approx 10^{-6}$ and $\beta^* \approx 10^{-5.5}$ in the cases of the viscosity ratio $r = 200$ and $r = 1000$,

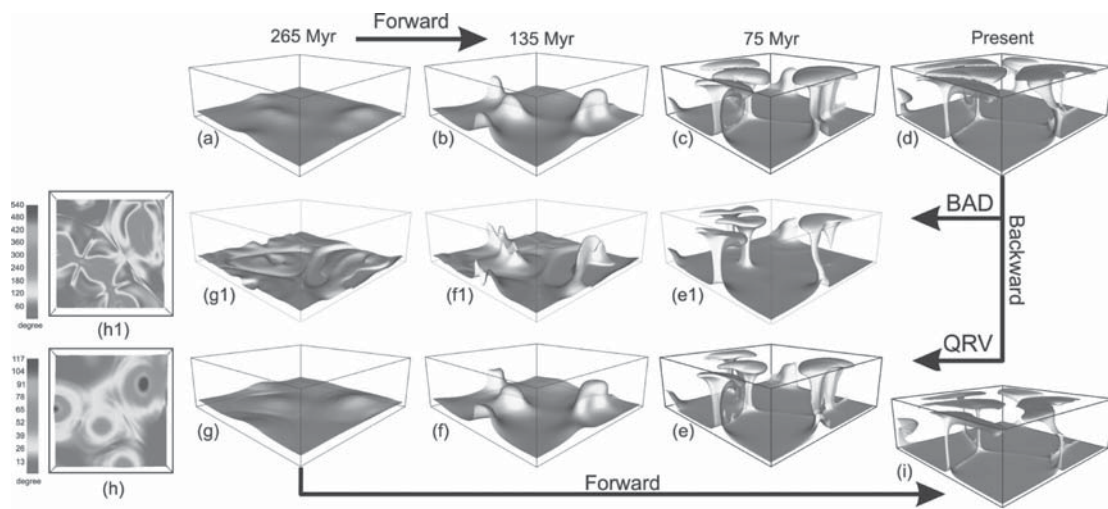


Fig. 8.10. Model of mantle plume evolution forward in time at successive times: (a–d) from 265 Myr ago to the present state of the plumes ($r = 20$). Assimilation of the mantle temperature and flow from the present state back to the geological past using the QRV (d–g; $\beta = 10^{-7}$) and BAD (d, e1–g1) methods. Verification of the QRV assimilation accuracy: forward model of the plume evolution starting from the initial (restored) state of the plumes (g) to their present state (i). Temperature residuals between the initial temperature for the forward model and the temperature assimilated to the same age using the QRV and BAD methods are presented in panels (h) and (h1), respectively. After Ismail-Zadeh *et al.* (2007). (In colour as Plate 6. See colour plates section.)

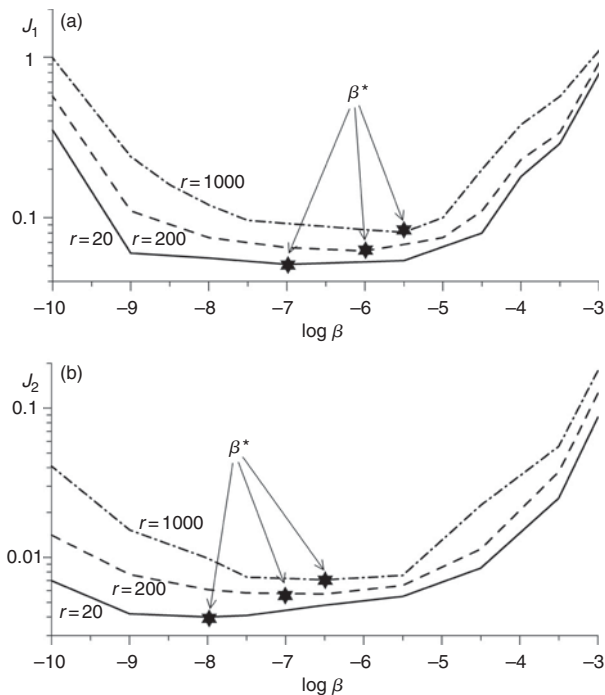


Fig. 8.11. Temperature misfit (a) J_1 and (b) J_2 as functions of the regularisation parameter β . The minimum of the temperature misfit is achieved at β^* , an optimal regularisation parameter. Solid curves: $r = 20$; dashed curves: $r = 200$; and dash-dotted curves: $r = 1000$. After Ismail-Zadeh *et al.* (2007).

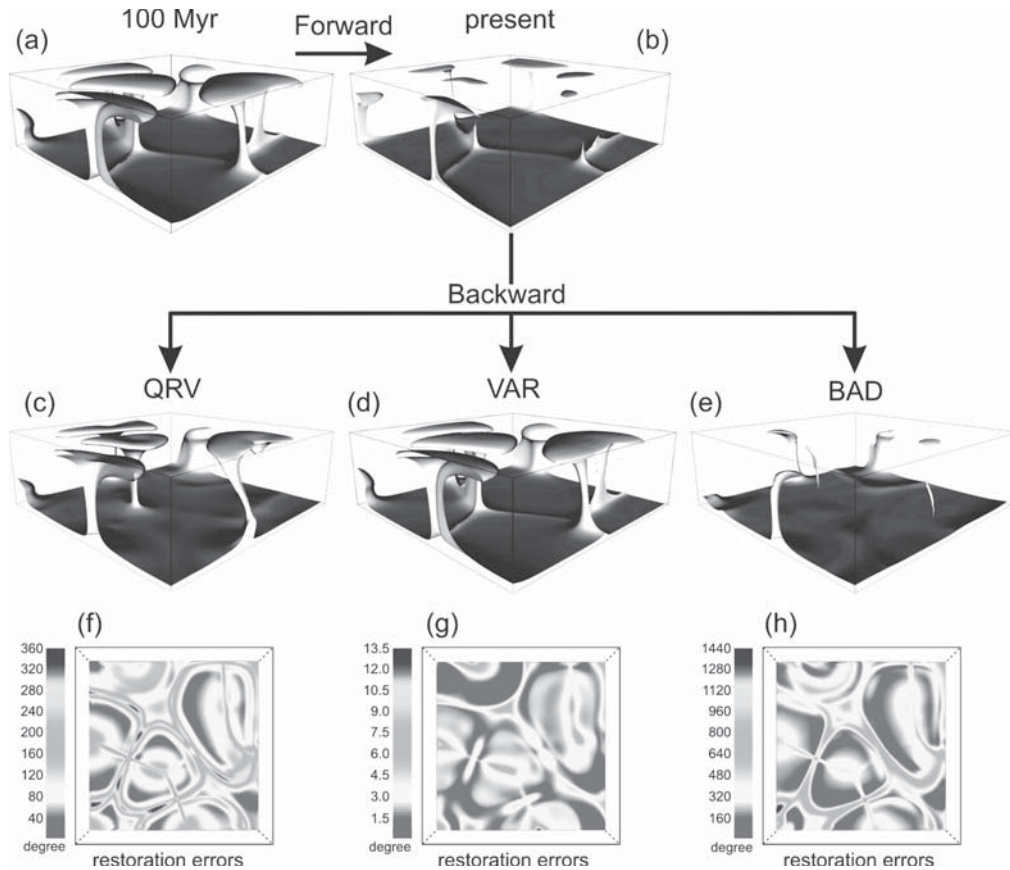


Fig. 8.12. Model of mantle plume diffusion forward in time (a and b; $r = 20$). Assimilation of the mantle temperature and flow to the time of 100 Myrs ago and temperature residuals between the present temperature model (b) and the temperature assimilated to the same age, using the QRV (c and f; $\beta = 10^{-7}$), VAR (d and g), and BAD (e and h) methods, respectively. After Ismail-Zadeh *et al.* (2007). (In colour as Plate 7. See colour plates section.)

respectively. Figure 8.11b illustrates the residual $J_2(\beta) = \|T_\beta(t_0, \cdot; T_\vartheta) - T_{\hat{\beta}}(t_0, \cdot; T_\vartheta)\|$ between the reconstructed temperature at $t_0 = 265$ Myr ago obtained for various values of β in the range $10^{-9} \leq \beta \leq 10^{-3}$ and $\hat{\beta} = \beta/2$. These results show the choice of the optimal value of the regularisation parameter using step 4b of the numerical algorithm for the QRV data assimilation (Section 8.8.3). In the case of $r = 20$ the parameter $\beta^* = \arg \min\{J_2(\beta) : \beta = \beta_k, k = 1, 2, \dots, 12\} \approx 10^{-8}$ provides the optimal accuracy for the solution; in the cases of $r = 200$ and $r = 1000$ the optimal accuracy is achieved at $\beta^* \approx 10^{-7}$ and $\beta^* \approx 10^{-6.5}$, respectively. Comparison of the temperature residuals for three values of the viscosity ratio r indicates that the residuals become larger as the viscosity ratio increases. The numerical experiments show that the algorithm for solving the inverse problem performs well when the regularisation parameter is in the range $10^{-8} \leq \beta \leq 10^{-6}$. For greater values, the solution of the inverse problem retains the stability but is less accurate. For $\beta < 10^{-9}$ the numerical procedure becomes unstable, and the computations must be stopped.

To compare how the techniques for data assimilation can restore the prominent state of the thermal plumes in the past from their ‘present’ weak state, a forward model was initially developed from the prominent state of the plumes (Fig. 8.12a) to their diffusive state in 100 Myr (Fig. 8.12b) using $50 \times 50 \times 50$ finite rectangular elements to approximate the vector velocity potential and a finite difference grid $148 \times 148 \times 148$ for approximation of temperature, velocity and viscosity. All other parameters of the model are the same.

The VAR method (Fig. 8.12d, g) provides the best performance for the diffused plume restoration. The BAD method (Fig. 8.12e, h) cannot restore the diffused parts of the plumes, because temperature is only advected backward in time. The QRV method (Fig. 8.12c, f) restores the diffused thermal plumes, meanwhile the restoration results are not so perfect as in the case of VAR method (compare temperature residuals in Fig. 8.12, panels f and g). Although the accuracy of the QRV data assimilation is lower compared with the VAR data assimilation, the QRV method does not require any additional smoothing of the input data and filtering of temperature noise as the VAR method does.

8.10 Application of the QRV method: restoration of descending lithosphere evolution

8.10.1 The Vrancea seismicity and the relic descending slab

Repeated large intermediate-depth earthquakes in the southeastern (SE-) Carpathians (the Vrancea region) cause destruction in Bucharest, the capital city of Romania, and shake central and eastern European cities several hundred kilometres away from the hypocentres of the events. The earthquake-prone Vrancea region (Fig. 8.13) is bounded to the north and north-east by the Eastern European platform (EEP), to the east by the Scythian platform (SCP), to the south-east by the North Dobrogea orogen (DOB), to the south and south-west by the Moesian platform (MOP), and to the north-west by the Transylvanian basin (TRB). The epicentres of the sub-crustal earthquakes in the Vrancea region are concentrated within a very small seismogenic volume about $70 \times 30 \text{ km}^2$ in planform and between depths of about 70 and 180 km. Below this depth the seismicity ends abruptly: one seismic event at 220 km depth is an exception (Onicescu and Bonjer, 1997).

The 1940 $M_W = 7.7$ earthquake gave rise to the development of a number of geodynamic models for this region. McKenzie (1972) suggested that this seismicity is associated with a relic slab sinking in the mantle and now overlain by continental crust. The 1977 large earthquake and later the 1986 and 1990 earthquakes again raised questions about the nature of the earthquakes. A seismic gap at depths of 40–70 km beneath Vrancea led to the assumption that the lithospheric slab had already detached from the continental crust (Fuchs *et al.*, 1979). Onicescu (1984) proposed that the intermediate-depth events are generated in a zone that separates the sinking slab from the neighbouring immobile part of the lithosphere rather than in the sinking slab itself. Linzer (1996) explained the nearly vertical position of the Vrancea slab as the final rollback stage of a small fragment of oceanic lithosphere. Various types of slab detachment or delamination (see, for example, Gırbacea and Frisch, 1998; Wortel and Spakman, 2000; Gvirtzman, 2002; Sperner *et al.*, 2005) have been

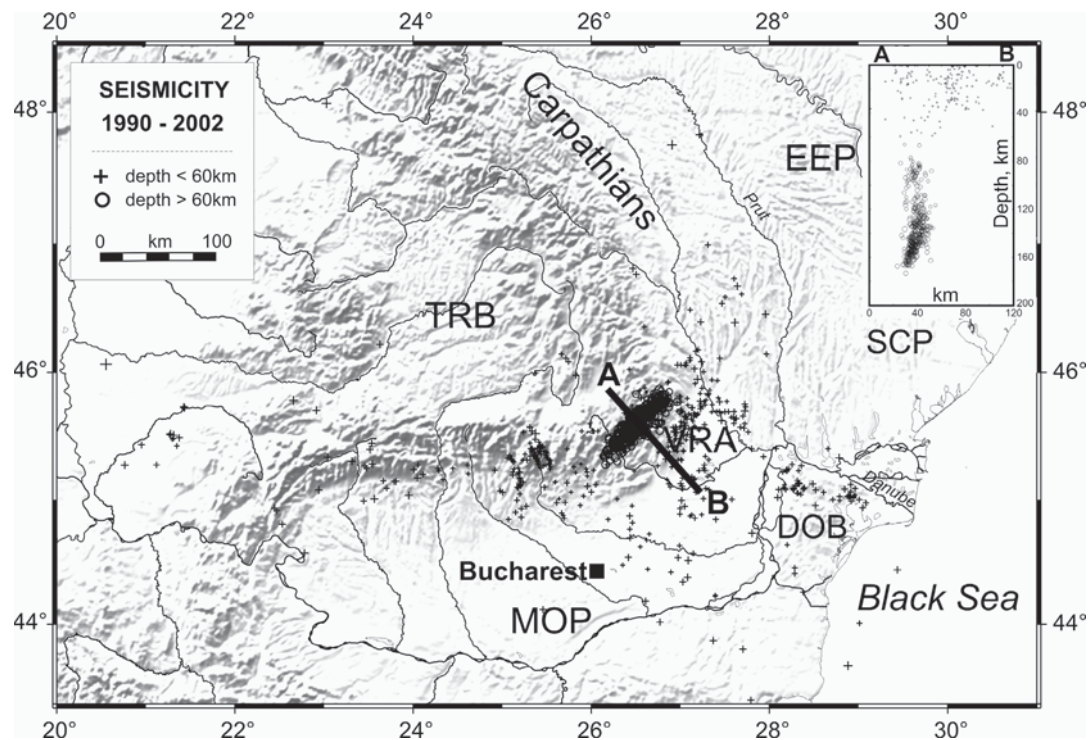


Fig. 8.13. Topography map of the SE-Carpathians and epicentres of Vrancea earthquakes (magnitude ≥ 3). The upper right panel presents hypocentres of the same earthquakes projected onto the NW-SE vertical plane AB. DOB, Dobrogea orogen; EEP, Eastern European platform; MOP, Moesian platform; SCP, Scythian platform; TRB, Transylvanian basin; and VRA, Vrancea. After Ismail-Zadeh *et al.* (2008).

proposed to explain the present-day seismic images of the descending slab. Cloetingh *et al.* (2004) argued in favour of the complex configuration of the underthrust lithosphere and its thermo-mechanical age as primary factors in the behaviour of the descending slab after continental collision. The origin of the descending lithosphere in the region, i.e. whether the Vrancea slab is oceanic or continental, is still under debate. Pana and Erdmer (1996) and Pana and Morris (1999) argued that because there is no geological evidence of Miocene oceanic crust in the eastern Carpathians, the descending lithosphere is likely to be thinned continental or transitional lithosphere.

The Neogene to Late Miocene (*c.* 11 Myr) evolution of the Carpathian region is mainly driven by the north-eastward, later eastward and south-eastward roll-back or slab retreat (Royden, 1988; Sperner *et al.*, 2001) into a Carpathians embayment, consisting of the last remnants of an oceanic or thinned continental domain attached to the European continent (see Balla, 1987; Csontos *et al.*, 1992). When the mechanically strong East-European and Scythian platforms started to enter the subduction zone, the buoyancy forces of the thick continental crust exceeded the slab pull forces and convergence stopped after only a short period of continental thrusting (Tarapoanca *et al.*, 2004; Sperner *et al.*, 2005). Continental convergence in the SE-Carpathians ceased about 11 Myr (Jiricek, 1979; Csontos *et al.*,

1992), and after that the lithospheric slab descended beneath the Vrancea region due to gravity. The hydrostatic buoyancy forces promote the sinking of the slab, but viscous and frictional forces resist the descent. The combination of these forces produces shear stresses at intermediate depths that are high enough to cause earthquakes (Ismail-Zadeh *et al.*, 2000a, 2005b).

In this section we present a quantitative model of the thermal evolution of the descending slab in the SE-Carpathians suggested by Ismail-Zadeh *et al.* (2008). The model is based on assimilation of present crust/mantle temperature and flow in the geological past using the QRV method. Mantle thermal structures are restored and analysed in the context of modern regional geodynamics.

8.10.2 Temperature model

Temperature is a key physical parameter controlling the density and rheology of the Earth's material and hence crustal and mantle dynamics. Besides direct measurements of temperature in boreholes in the shallow portion of the crust, there are no direct measurements of deep crustal and mantle temperatures, and therefore the temperatures must be estimated indirectly from seismic wave anomalies, geochemical data and surface heat flow observations.

Ismail-Zadeh *et al.* (2005a, 2008) developed a model of the present crustal and mantle temperature beneath the SE-Carpathians by using the most recent high-resolution seismic tomography image (map of the anomalies of P -wave velocities) of the lithosphere and asthenosphere in the region (Martin *et al.*, 2005, 2006). The tomography image shows a high velocity body beneath the Vrancea region and the Moesian platform interpreted as the subducted lithospheric slab (Martin *et al.*, 2006). The seismic tomographic model of the region consists of eight horizontal layers of different thickness (15 km up to 70 km) starting from the depth of 35 km and extending down to a depth of 440 km. Each layer of about $1000 \times 1000 \text{ km}^2$ is subdivided horizontally into $16 \times 16 \text{ km}^2$ blocks. To restrict numerical errors in our data assimilation we smooth the velocity anomaly data between the blocks and the layers using a spline interpolation. Ismail-Zadeh *et al.* (2005a) converted seismic wave velocity anomalies into temperature considering the effects of mantle composition, anelasticity, and partial melting on seismic velocities. The temperature in the crust is constrained by measurements of surface heat flux corrected for palaeoclimate changes and for the effects of sedimentation (Demetrescu *et al.*, 2001).

Depth slices of the present temperature model are illustrated in Fig. 8.14. The pattern of resulting mantle temperature anomalies (predicted temperature minus background temperature) is similar to the pattern of observed P -wave velocity anomalies (Martin *et al.*, 2006), but not an exact copy because of the non-linear inversion of the seismic anomalies to temperature. The low temperatures are associated with the high-velocity body beneath the Vrancea region (VRA) and the East European platform (EEP) and are already visible at depths of 50 km. The slab image becomes clear at 70–110 km depth as a NE–SW oriented cold anomaly. With increasing depth (110–200 km depth) the thermal image of the slab broadens in NW–SE direction. The orientation of the cold body changes from NE–SW to N–S below the depth of 200 km. The slab extends down to 280–320 km depth beneath

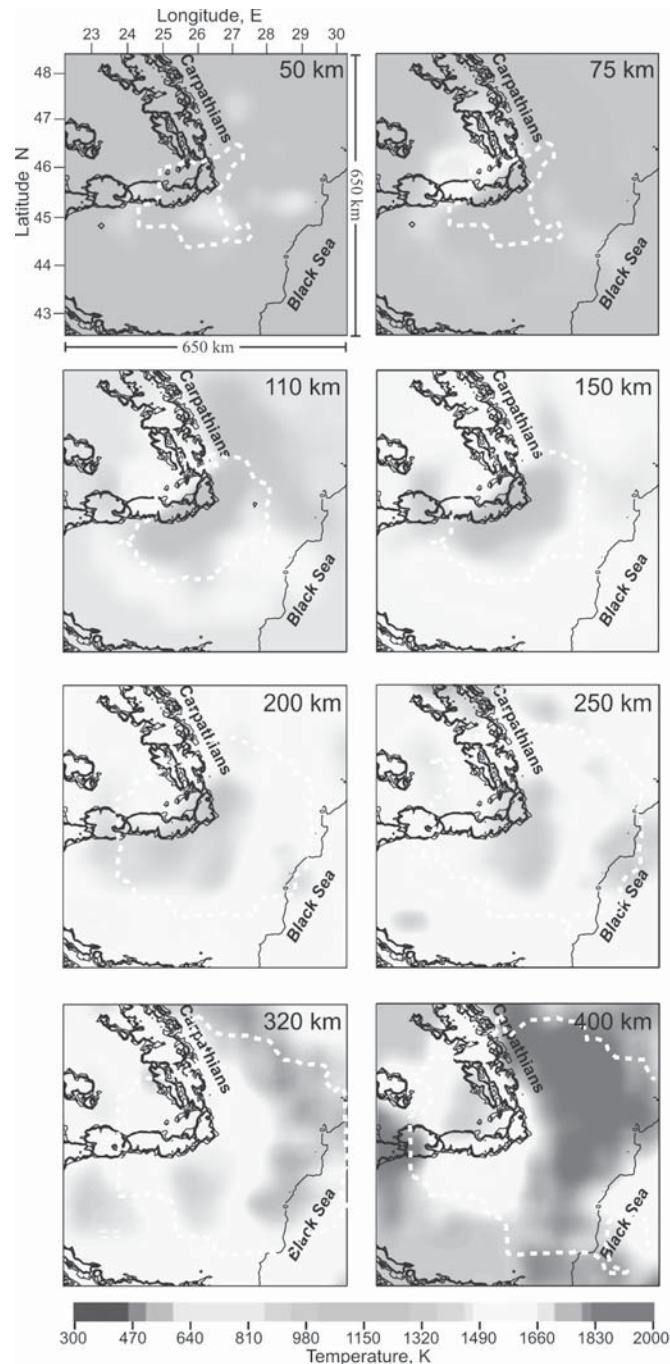


Fig. 8.14. Present temperature model as the result of the inversion of the P -wave velocity model. Theoretically well-resolved regions are bounded by dashed line (see text and Martin *et al.*, 2006). Each slice presents a part of the horizontal section of the model domain Ω corresponding to $[x_1 = 177.5 \text{ km}, x_1 = 825.5 \text{ km}] \times [x_2 = 177.5 \text{ km}, x_2 = 825.5 \text{ km}]$, and the isolines present the surface topography (also in Figs. 8.15 and 8.17). After Ismail-Zadeh *et al.* (2008). (In colour as Plate 8. See colour plates section.)

the Vrancea region itself. A cold anomaly beneath the Transylvanian Basin is estimated at depths of 370–440 km. According to Wortel and Spakman (2000) and Martin *et al.* (2006) this cold material can be interpreted as a remnant of subducted lithosphere detached during the Miocene along the Carpathian Arc and residing within the upper mantle transition zone. High temperatures are predicted beneath the Transylvanian Basin (TRB) at about 70–110 km depth. Two other high temperature regions are found at 110–150 km depth below the Moesian platform (MOP) and deeper than 200 km under the EEP and the Dobrogea orogen (DOB), which might be correlated with the regional lithosphere/asthenosphere boundary.

8.10.3 QRV data assimilation

To minimise boundary effects, the studied region ($650 \times 650 \text{ km}^2$ and 440 km deep, see Fig. 8.14) has been bordered horizontally by a 200 km area and extended vertically to the depth of 670 km. Therefore, a rectangular domain $\Omega = [0, l_1 = 1050 \text{ km}] \times [0, l_2 = 1050 \text{ km}] \times [0, h = 670 \text{ km}]$ is considered for assimilation of present temperature and mantle flow beneath the SE-Carpathians.

Our ability to reverse mantle flow is limited by our knowledge of past movements in the region, which are well constrained in only some cases. In reality, the Earth's crust and lithospheric mantle are driven by mantle convection and the gravitational pull of dense descending slabs. However, when a numerical model is constructed for a particular region, external lateral forces can influence the regional crustal and uppermost mantle movements. Yet in order to make useful predictions that can be tested geologically, a time-dependent numerical model should include the history of surface motions. Since this is not currently achievable in a dynamical way, it is necessary to prescribe surface motions by using velocity boundary conditions.

The simulations are performed backward in time for a period of 22 Myr. Perfect slip conditions are assumed at the vertical and lower boundaries of the model domain. For the first 11 Myr (starting from the present time), when the rates of continental convergence were insignificant (Jiricek, 1979; Csontos *et al.*, 1992), no velocity is imposed at the surface, and the conditions at the upper boundary are free slip. The north-westward velocity is imposed in the portion of the upper model boundary (Fig. 8.15a) for the time interval from 11 Myr to 16 Myr and the westward velocity in the same portion of the boundary (Fig. 8.15b) for the interval from 16 Myr to 22 Myr. The velocities are consistent with the direction and rates of the regional convergence in the Early and Middle Miocene (Morley, 1996; Fügenschuh and Schmid, 2005; Sperner *et al.*, 2005). The effect of the surface loading due to the Carpathian Mountains is not considered, because this loading would have insignificant influence on the dynamics of the region (as was shown in two-dimensional models of the Vrancea slab evolution; Ismail-Zadeh *et al.*, 2005b).

The heat flux through the vertical boundaries of the model domain Ω is set to zero. The upper and lower boundaries are assumed to be isothermal surfaces. The present temperature above 440 km depth is derived from the seismic velocity anomalies and heat flow data. The adiabatic geotherm for potential temperature 1750 K (Katsura *et al.*, 2004) was used to define the present temperature below 440 km (where seismic tomography data are not

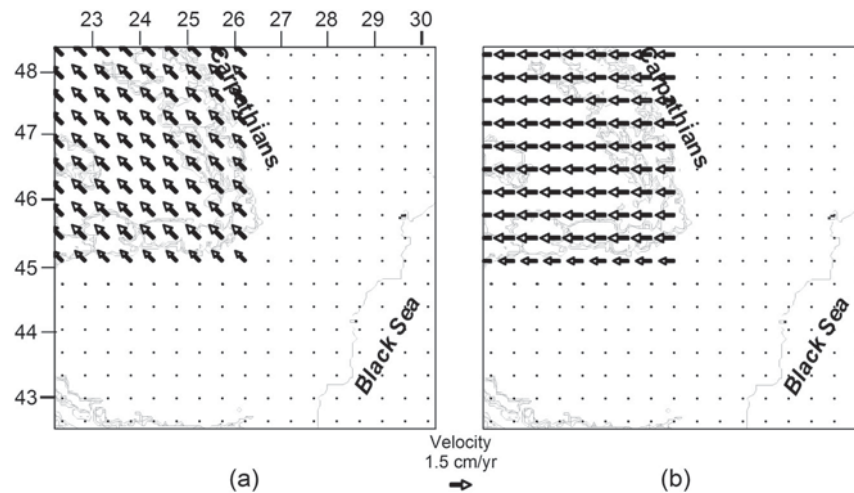


Fig. 8.15.

Surface velocity imposed on the part of the upper boundary of the model domain (see the caption of Fig. 8.14) in data assimilation modelling for the time interval from 11 Myr to 16 Myr ago (a) and for that from 16 Myr to 22 Myr ago (b). After Ismail-Zadeh *et al.* (2008).

available). Equations (8.36)–(8.49) with the specified boundary and initial conditions are solved numerically.

To estimate the accuracy of the results of data assimilation, the temperature and mantle flow restored to the time of 22 Myr ago were employed as the initial condition for a model of the slab evolution forward in time; the model was run to the present; and the temperature residual (the difference between the present temperature and that predicted by the forward model with the restored temperature as an initial temperature distribution) was analysed subsequently. The maximum temperature residual does not exceed 50 K.

A sensitivity analysis was performed to understand how stable is the numerical solution to small perturbations of input (present) temperatures. The model of the present temperature (Section 8.10.2) has been perturbed randomly by 0.5% to 2% and then assimilated to the past to find the initial temperature. A misfit between the initial temperatures related to the perturbed and unperturbed present temperature is rather small (2% to 4%), which proves that the solution is stable. The numerical models, with a spatial resolution of $7 \text{ km} \times 7 \text{ km} \times 5 \text{ km}$, were run on parallel computers. The accuracy of the numerical solutions has been verified by several tests, including grid and total mass changes (Ismail-Zadeh *et al.*, 2001a).

8.10.4 What the past tells us

We discuss here the results of assimilation of the present temperature model beneath the SE-Carpathians into Miocene times. Although there is some evidence that the lithospheric slab was already partly subducted some 75 Myr ago (Sandulescu, 1988), the assimilation interval was restricted to the Miocene, because the pre-Miocene evolution of the descending slab, as well as the regional horizontal movements, are poorly known. Incorporation of insufficiently

accurate data into the assimilation model could result in incorrect scenarios of mantle and lithosphere dynamics in the region. Moreover, to restore the history of pre-Miocene slab subduction, a high-resolution seismic tomography image of the deeper mantle is required (the present image is restricted to the depth of 440 km).

Early Miocene subduction beneath the Carpathian arc and the subsequent gentle continental collision transported cold and dense lithospheric material into the hotter mantle. Figure 8.16 presents the 3-D thermal image of the slab and pattern of contemporary flow induced by the descending slab. Note that the direction of the flow is reversed, because we solve the problem backward in time: cold slabs move upward during the numerical modelling. The 3-D flow is rather complicated: toroidal (in horizontal planes) flow at depths between about 100 km and 200 km coexists with poloidal (in vertical planes) flow.

The relatively cold (blue to dark green) region seen at depths of 40 km to 230 km (Fig. 8.17b) can be interpreted as the earlier evolutionary stages of the lithospheric slab. The slab is poorly visible at shallow depth in the model of the present temperature (Fig. 8.17a). Since active subduction of the lithospheric slab in the region ended in Late Miocene times and earlier rates of convergence were low before it, Ismail-Zadeh *et al.* (2006) argue that the cold slab, descending slowly at these depths, has been warmed up, and its thermal shape has faded due to heat diffusion. Thermal conduction in the shallow Earth (where viscosity is high) plays a significant part in heat transfer compared to thermal convection. The deeper we look in the region, the larger are the effects of thermal advection compared to conduction: the lithosphere has moved upwards to the place where it had been in Miocene times. Below 230 km depth the thermal roots of the cold slab are clearly visible in the present temperature model (Figs. 8.14, 8.16 and 8.17a), but they are almost invisible in Fig. 8.17b and in Fig. 8.18 of the models of the assimilated temperature, because the slab did not reach these depths in Miocene times.

The geometry of the restored slab clearly shows two parts of the sinking body (Figs. 8.17b and 8.18). The NW–SE oriented part of the body is located in the vicinity of the boundary between the EEP and Scythian platform (SCP) and may be a relic of cold lithosphere that has travelled eastward. Another part has a NE–SW orientation and is associated with the present descending slab. An interesting geometrical feature of the restored slab is its curvature beneath the SE-Carpathians. In Miocene times the slab had a concave surface confirming the curvature of the Carpathian arc down to depths of about 60 km. At greater depths the slab changed its shape to that of a convex surface and split into two parts at a depth of about 200 km. Although such a change in slab curvature is visible neither in the model of the present temperature nor in the seismic tomography image, most likely because of slab warming and heat diffusion, we suggest that the convex shape of the slab is likely to be preserved at the present time. Ismail-Zadeh *et al.* (2008) proposed that this change in the geometry of the descending slab can cause stress localisation due to slab bending and subsequent stress release resulting in earthquakes, which occur at depths of 70–180 km in the region.

Moreover, the north–south (NS)-oriented cold material visible at the depths of 230 km to 320 km (Figs. 8.14 and 8.17a) does not appear as a separate (from the NE–SW-oriented slab) body in the models of Miocene time. Instead, it looks more like two differently oriented branches of the SW-end of the slab at 60–130 km depth (visible in Figs. 8.17b and 8.18).

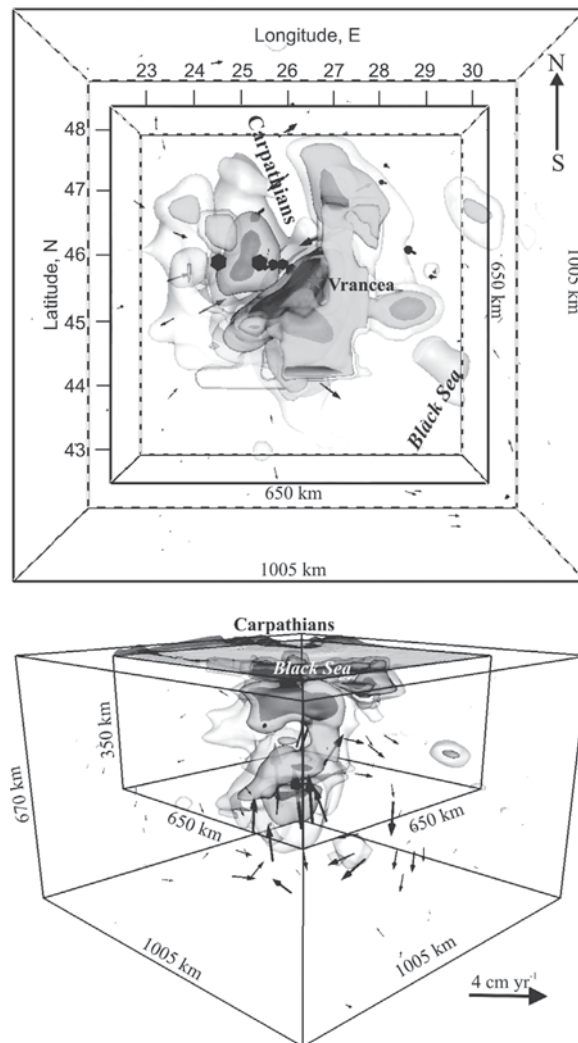


Fig. 8.16. A 3-D thermal shape of the Vrancea slab and contemporary flow induced by the descending slab beneath the SE-Carpathians. Upper panel: top view. Lower panel: side view from the SE toward NW. Arrows illustrate the direction and magnitude of the flow. The marked sub-domain of the model domain presents the region around the Vrancea shown in Fig. 8.17 (in horizontal slices) and in Fig. 8.18. The surfaces marked by blue, dark cyan and light cyan illustrate the surfaces of 0.07, 0.14 and 0.21 temperature anomaly δT , respectively, where $\delta T = (T_{hav} - T)/T_{hav}$ and T_{hav} is the horizontally averaged temperature. The top surface presents the topography, and the red star marks the location of the intermediate-depth earthquakes. After Ismail-Zadeh *et al.* (2008). (In colour as Plate 9. See colour plates section.)

Therefore, the results of the assimilation of the present temperature model to Miocene time provide a plausible explanation for the change in the spatial orientation of the slab from NE–SW to NS beneath 200 km observed in the seismic tomography image (Martin *et al.*, 2006).

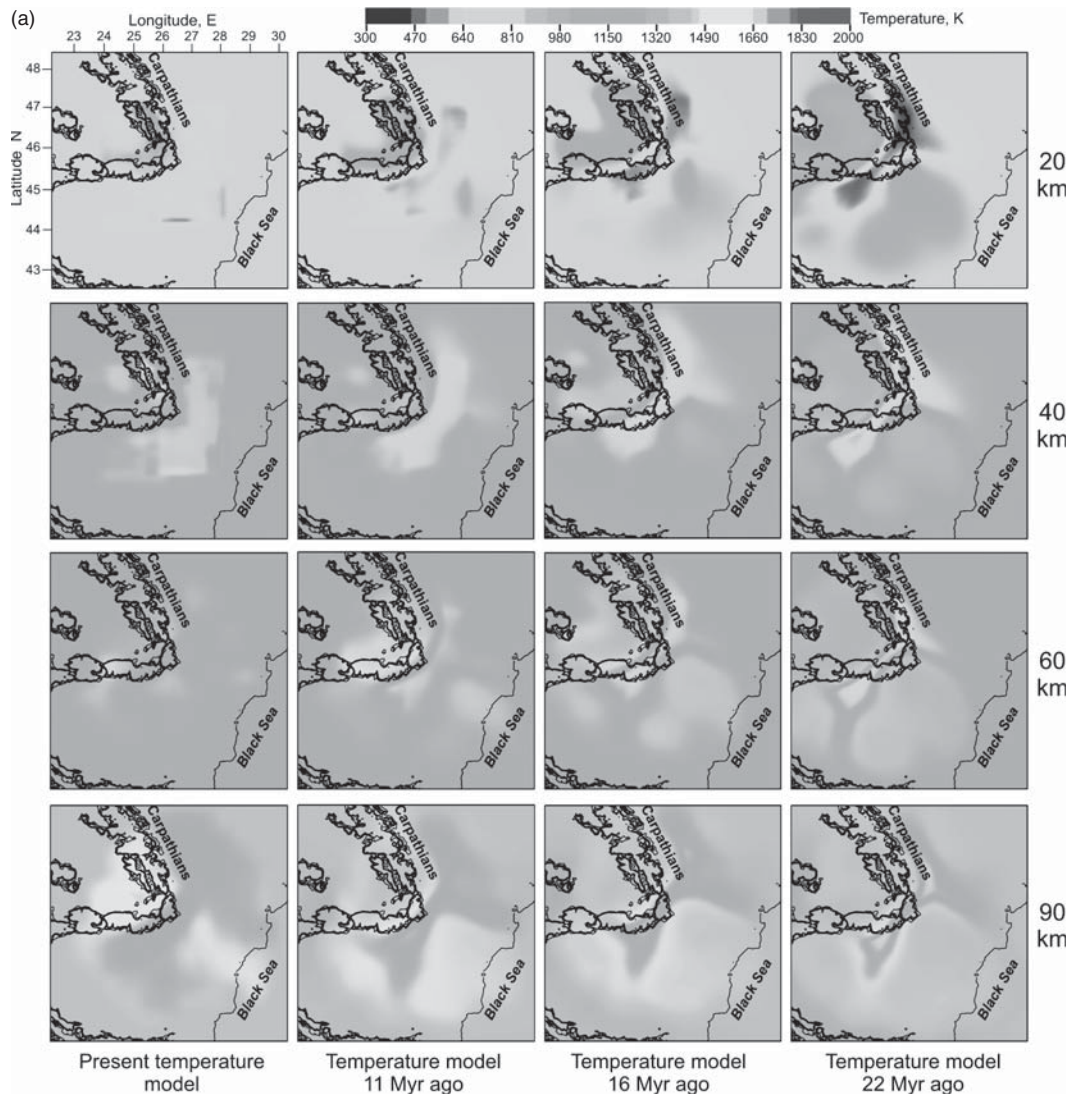


Fig. 8.17. Thermal evolution of the crust and mantle beneath the SE-Carpathians. Horizontal sections of temperature obtained by the assimilation of the present temperature to the Miocene times. After Ismail-Zadeh *et al.* (2008). (In colour as Plate 10. See colour plates section.)

The slab bending might be related to a complex interaction between two parts of the sinking body and the surrounding mantle. The sinking body displaces the mantle, which, in its turn, forces the slab to deform due to corner (toroidal) flows different within each of two sub-regions (to NW and to SE from the present descending slab). Also, the curvature of the descending slab can be influenced by slab heterogeneities due to variations in its thickness and viscosity (Cloetingh *et al.*, 2004; Morra *et al.*, 2006).

Martin *et al.* (2006) interpret the negative velocity anomalies NW of the present slab at depths between 70 km and 110 km (see the relevant temperature slices in Figs. 8.14 and 8.17a) as a shallow asthenospheric upwelling associated with possible slab rollback. Also, they mention partial melting as an additional contribution to the reduction of seismic

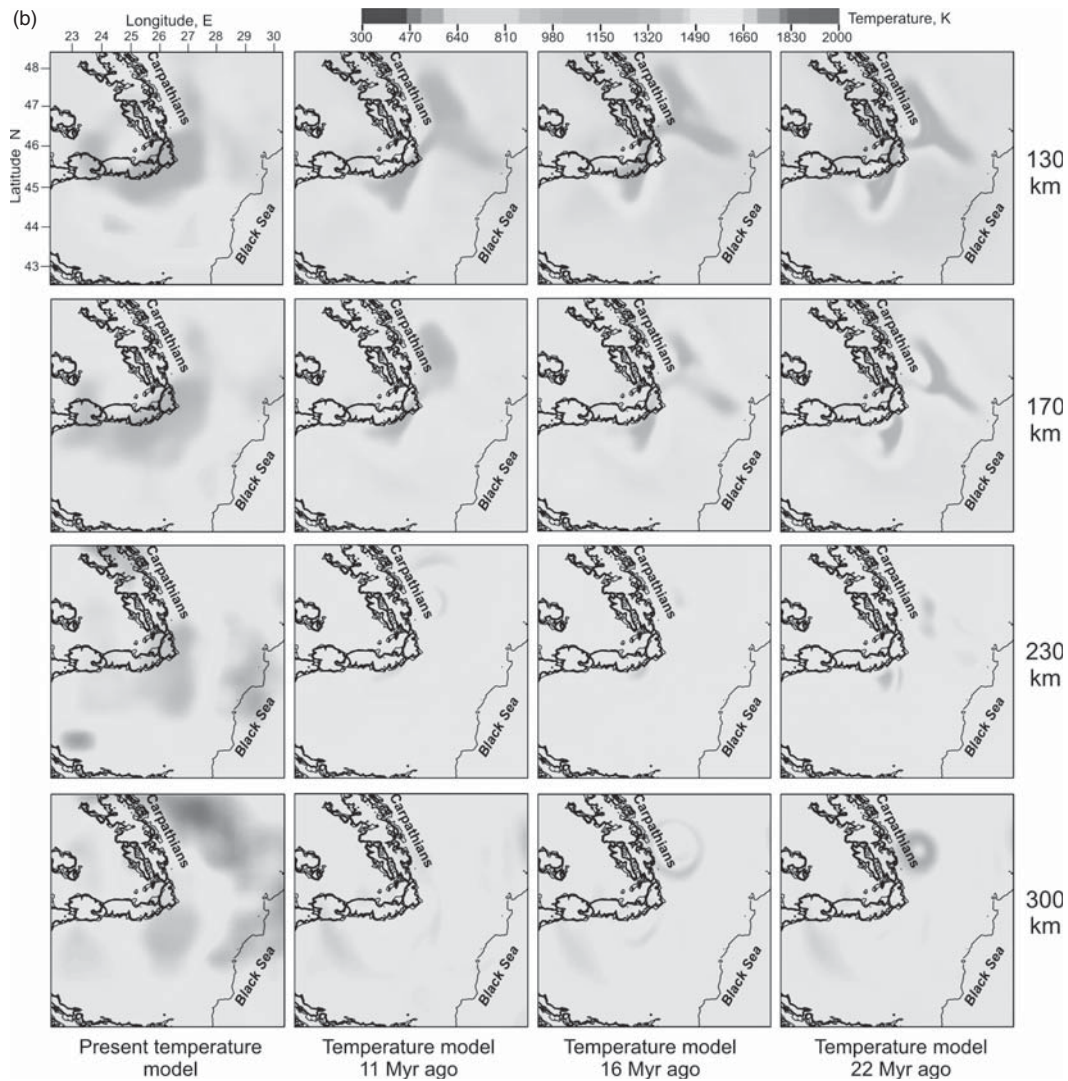


Fig. 8.17. (Continued)

velocities at these depths. The results of our assimilation show that the descending slab is surrounded by a border of hotter rocks at depths down to about 250 km. The rocks could be heated owing to partial melting as a result of slab dehydration. Although the effects of slab dehydration or partial melting were not considered in the modelling, the numerical results support the hypothesis of dehydration of the descending lithosphere and its partial melting as the source of reduction of seismic velocities at these depths and probably deeper (see temperature slices at the depths of 130–220 km). Alternatively, the hot anomalies beneath the Transylvanian basin and partly beneath the Moesian platform could be dragged down by the descending slab since the Miocene times, and therefore, the slab was surrounded by the hotter rocks. Using numerical experiments, Honda *et al.* (2007) showed recently how the lithospheric plate subducting beneath the Honshu Island in Japan dragged down a hot anomaly adjacent to the plate. Some areas of high temperature at depths below 280 km

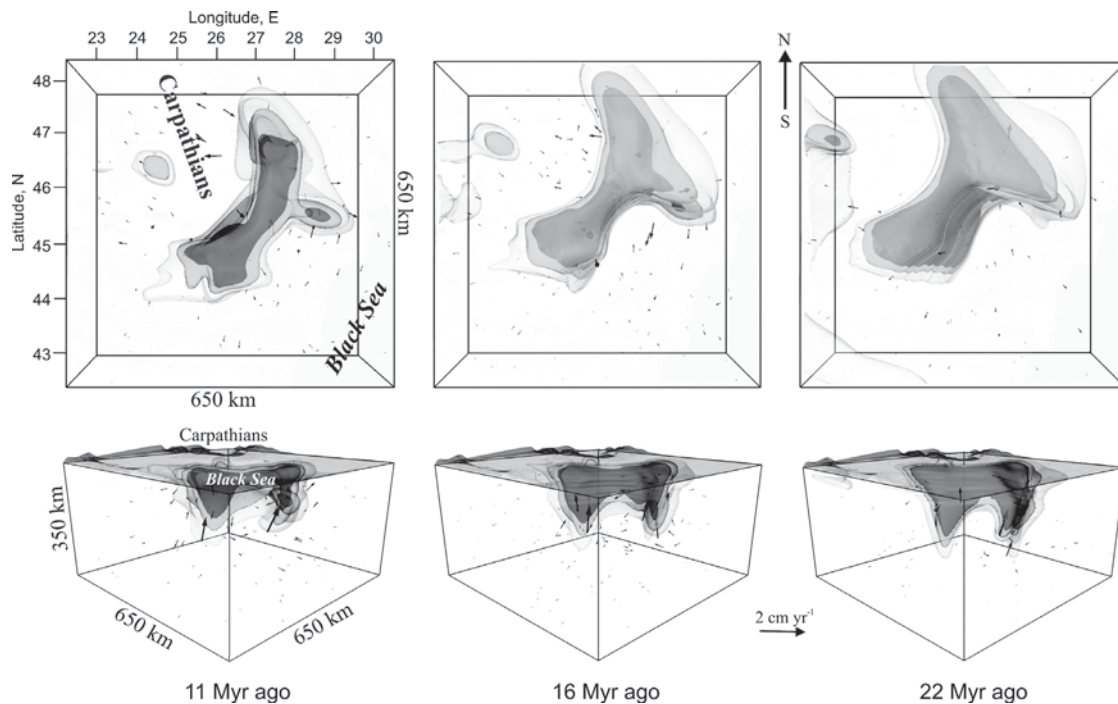


Fig. 8.18. Snapshots of the 3-D thermal shape of the Vrancea slab and pattern of mantle flow beneath the SE-Carpathians in the Miocene times. See Fig. 8.16 for other notations. After Ismail-Zadeh *et al.* (2008). (In colour as Plate 11. See colour plates section.)

can be associated with mantle upwelling in the region. High-temperature anomalies are not clearly visible in the restored temperatures at these depths, because the upwelling was likely not active in Miocene times.

The numerical results were compared with that obtained by the backward advection of temperature (using the BAD method). Figure 8.19 (dashed curve) shows that the maximum temperature residual is about 360 K. The neglect of heat diffusion leads to an inaccurate restoration of mantle temperature, especially in the areas of low temperature and high viscosity. The similar results for the BAD data assimilation have been obtained in the synthetic case study (see Fig. 8.12e and h).

8.10.5 Limitations and uncertainties

There is a major physical limitation of the restoration of mantle structures. If a thermal feature created, let us say, several hundred million years ago has completely diffused away by the present, it is impossible to restore the feature, which was more prominent in the past. The time to which a present thermal structure in the upper mantle can be restored should be restricted by the characteristic thermal diffusion time, the time when the temperatures of the evolved structure and the ambient mantle are nearly indistinguishable (Ismail-Zadeh *et al.*, 2004a). The time (t) for restoration of seismic thermal structures depends on depth

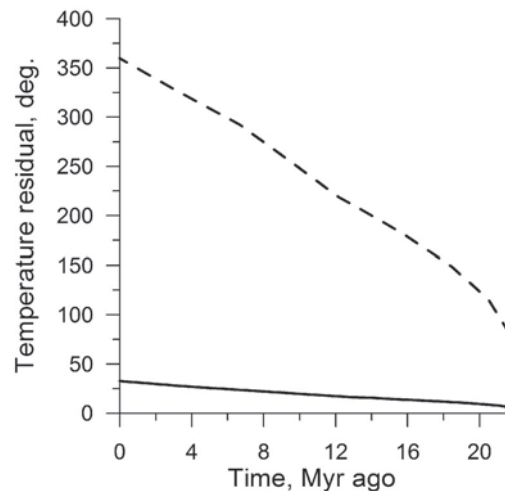


Fig. 8.19.

Temperature misfit in the model of the descending lithospheric slab beneath the southeastern Carpathians. The misfit is defined as an integral difference between the temperature assimilated to any time $t \in [\text{present}, 22 \text{ Myr ago}]$ and that predicted by the forward model (8.21)–(8.26) to the same time assuming the assimilated temperature 22 Myr ago as the initial condition for the forward model. Solid and dashed curves present the misfits for the cases of temperature assimilation using the QRV and BAD methods, respectively.

(d) of seismic tomography images and can be roughly estimated as $t = d/v$, where v is the average vertical velocity of mantle flow. For example, the time for restoration of the Vrancea slab evolution in the studied models should be less than about 80 Myr, considering $d = 400 \text{ km}$ and $v \approx 0.5 \text{ cm yr}^{-1}$.

Other sources of uncertainty in the modelling of mantle temperature in the SE-Carpathians come from the choice of mantle composition (Nitoi *et al.*, 2002; Seghedi *et al.*, 2004; Szabó *et al.*, 2004), the seismic attenuation model (Popa *et al.*, 2005; Weidle *et al.*, 2007), and poor knowledge of the presence of water at mantle depths. The drop of electrical resistivity below $1 \Omega \text{ m}$ (Stanica and Stanica, 1993) can be an indicator of the presence of fluids (due to dehydration of mantle rocks) below the SE-Carpathians; however, the information is very limited and cannot be used in quantitative modelling.

Viscosity is an important physical parameter in numerical modelling of mantle dynamics, because it influences the stress state and results in strengthening or weakening of Earth's material. Though it is the least-known physical parameter of the model, the viscosity of the Vrancea slab was constrained by observations of the regional strain rates (Ismail-Zadeh *et al.*, 2005a).

The geometry of the mantle structures changes with time, diminishing the degree of surface curvature of the structures. Like Ricci flow, which tends to diffuse regions of high curvature into ones of lower curvature (Hamilton, 1982; Perelman, 2002), heat conduction smoothes the complex thermal surfaces of mantle bodies with time. Present seismic tomography images of mantle structures do not allow definition of the sharp shapes of these structures. Assimilation of mantle temperature and flow to the geological past instead provides a quantitative tool to restore thermal shapes of prominent structures in the past from

their diffusive shapes at present. High-resolution experiments on seismic wave attenuation, improved knowledge of crustal and mantle mineral composition, accurate GPS measurements of regional movements, and precise geological palaeoreconstructions of crustal movements will assist to refine the present models and our knowledge of the regional thermal evolutions. The basic knowledge we have gained from the case studies is the dynamics of the Earth's interior in the past, which could result in its present dynamics.

8.11 Comparison of data assimilation methods

We compare the VAR, QRV and BAD methods in terms of solution stability, convergence, and accuracy, time interval for data assimilation, analytical and algorithmic works, and computer performance (see Tables 8.1–8.3). The VAR data assimilation assumes that the direct and adjoint problems are constructed and solved iteratively forward in time. The structure of the adjoint problem is identical to the structure of the original problem, which considerably simplifies the numerical implementation. However, the VAR method imposes some requirements for the mathematical model (i.e. a derivation of the adjoint problem). Moreover, for an efficient numerical implementation of the VAR method, the error level of the computations must be adjusted to the parameters of the algorithm, and this complicates computations.

The QRV method allows employing sophisticated mathematical models (because it does not require derivation of an adjoint problem as in the VAR data assimilation) and hence expands the scope for applications in geodynamics (e.g. thermo-chemical convection, phase transformations in the mantle). It does not require that the desired accuracy of computations be directly related to the parameters of the numerical algorithm. However, the regularising operators usually used in the QRV method enhance the order of the system of differential equations to be solved.

The BAD is the simplest method for data assimilation in models of mantle dynamics, because it does not require any additional work (neither analytical nor computational). The major difference between the BAD method and two other methods (VAR and QRV methods) is that the BAD method is by design expected to work (and hence can be used) *only* in advection-dominated heat flow. In the regions of high temperature/low mantle viscosity, where heat is transferred mainly by convective flow, the use of the BAD method is justified, and the results of numerical reconstructions can be considered to be satisfactory. Otherwise, in the regions of conduction-dominated heat flow (due to either high mantle viscosity or high conductivity of mantle rocks), the use of the BAD method cannot guarantee any similarity of reconstructed structures. If mantle structures are diffused significantly, the remaining features of the structures can be only backward advected with the flow.

The comparison between the data assimilation methods is summarised in Table 8.2 in terms of a quality of numerical results. The quality of the results is defined here as a relative (not absolute) measure of their accuracy. The results are good, satisfactory or poor compared with other methods for data assimilation considered in this study. The numerical results of the reconstructions for both synthetic and geophysical case studies show the comparison quantitatively.

Table 8.1. Comparison of methods for data assimilation in models of mantle dynamics

	QRV method	VAR method	BAD method
Method	Solving the regularised backward heat problem with respect to parameter β	Iterative sequential solving of the direct and adjoint heat problems	Solving of heat advection equation backward in time
Solution's stability	Stable for parameter β to numerical errors (see text; also in ¹) and conditionally stable for parameter β to arbitrarily assigned initial conditions (numerically ²)	Conditionally stable to numerical errors depending on the number of iterations (theoretically ³) and unstable to arbitrarily assigned initial conditions (numerically ⁴)	Stable theoretically and numerically
Solution's convergence	Numerical solution to the regularised backward heat problem converges to the solution of the backward heat problem in the special class of admissible solutions ⁵	Numerical solution converges to the exact solution in the Hilbert space ⁶	Not applied
Solution's accuracy ⁷	Acceptable accuracy for both synthetic and geophysical data	High accuracy for synthetic data	Low accuracy for both synthetic and geophysical data in conduction-dominated mantle flow
Time interval for data assimilation ⁸	Limited by the characteristic thermal diffusion time	Limited by the characteristic thermal diffusion time and the accuracy of the numerical solution	No specific time limitation; depends on mantle flow intensity
Analytical work	Choice of the regularising operator	Derivation of the adjoint problem	No additional analytical work
Algorithmic work	New solver for the regularised equation should be developed	No new solver should be developed	Solver for the advection equation is to be used

¹Lattes and Lions, 1969; ²see Fig. 8.11 and relevant text; ³Ismail-Zadeh *et al.*, 2004a; ⁴Ismail-Zadeh *et al.*, 2006; ⁵Tikhonov and Arsenin, 1977; ⁶Tikhonov and Samarskii, 1990; ⁷see Table 8.2; ⁸see text for details.

Table 8.2. Quality of the numerical results obtained by different methods for data assimilation

Quality	Synthetic data		Geophysical data	
	Advection-dominated regime	Diffusion-dominated region	Advection-dominated regime	Diffusion-dominated region
Good	VAR	VAR	—	—
Satisfactory	QRV, BAD	QRV	QRV, BAD	QRV
Poor	—	BAD	—	BAD

Table 8.3. Performance of data assimilation methods

Method	CPU time (circa, in s)		
	Solving the Stokes problem using $50 \times 50 \times 50$ finite elements	Solving the backward heat problem using $148 \times 148 \times 148$ finite difference mesh	Total
BAD	180	2.5	182.5
QRV	100 to 180	3	103 to 183
VAR	360	$1.5 n$	$360 + 1.5 n$

The time interval for the VAR data assimilation depends strongly on smoothness of the input data and the solution. The time interval for the BAD data assimilation depends on the intensity of mantle convection: it is short for conduction-dominated heat transfer and becomes longer for advection-dominated heat flow. In the absence of thermal diffusion the backwards advection of a low-density fluid in the gravity field will finally yield a uniformly stratified, inverted density structure, where the low-density fluid overlain by a dense fluid spreads across the lower boundary of the model domain to form a horizontal layer. Once the layer is formed, information about the evolution of the low-density fluid will be lost, and hence any forward modelling will be useless, because no information on initial conditions will be available (Ismail-Zadeh *et al.* 2001b; Kaus and Podladchikov 2001).

The QRV method can provide stable results within the characteristic thermal diffusion time interval. However, the length of the time interval for QRV data assimilation depends on several factors. Let us explain this by the example of heat conduction equation (8.27). Assume that the solution to the backward heat conduction equation with the boundary conditions (8.28) and the initial condition $T(t = t^*, x) = T^*(x)$ satisfies the inequality $\|\partial^4 T / \partial x^4\| \leq L_d$ at any time t . This strong additional requirement can be considered as the requirement of sufficient smoothness of the solution and initial data. Considering the regularised backward heat conduction equation (8.31) with the boundary conditions (8.32)–(8.33) and the input temperature $T_\beta(t = t^*, x) = T_\beta^*(x)$ and assuming that $\|T_\beta^* - T^*\| \leq \delta$, Samarskii and Vabishchevich (2004) estimated the temperature misfit between the solution $T(t, x)$ to the backward heat conduction problem and the solution $T_\beta(t, x)$ to the regularised

backward heat conduction equation:

$$\|T(t, x) - T_\beta(t, x)\| \leq \tilde{C}\delta \exp[\beta^{-1/2}(t^* - t)] + \beta L_d t, \quad 0 \leq t \leq t^*, \quad (8.53)$$

where constant \tilde{C} is determined from the *a priori* known parameters of the backward heat conduction problem. For the given regularisation parameter β , errors in the input data δ , and smoothness parameter L_d , it is possible to evaluate the time interval $0 \leq t \leq t^*$ of data assimilation for which the temperature misfit would not exceed a prescribed value.

Computer performance of the data assimilation methods can be estimated by a comparison of CPU times for solving the inverse problem of thermal convection. Table 8.3 lists the CPU times required to perform one time-step computations on 16 processors. The CPU time for the case of the QRV method is presented for a given regularisation parameter β ; in general, the total CPU time increases by a factor of \mathfrak{N} , where \mathfrak{N} is the number of runs required to determine the optimal regularisation parameter β^* . The numerical solution of the Stokes problem (by the conjugate gradient method) is the most time consuming calculation: it takes about 180 s to reach a high accuracy in computations of the velocity potential. The reduction in the CPU time for the QRV method is attained by employing the velocity potential computed at β_i as an initial guess function for the conjugate gradient method to compute the vector potential at β_{i+1} . An application of the VAR method requires to compute the Stokes problem twice to determine the ‘advected’ and ‘true’ velocities (Ismail-Zadeh *et al.*, 2004a). The CPU time required to compute the backward heat problem using the TVD solver (Section 7.9) is about 3 s in the case of the QRV method and 2.5 s in the case of the BAD method. For the VAR case, the CPU time required to solve the direct and adjoint heat problems by the semi-Lagrangian method (Section 7.8) is $1.5 \times n$, where n is the number of iterations in the gradient method (Eq. (8.15)) used to minimise the cost functional (Eq. (8.14)).

8.12 Errors in forward and backward modelling

A numerical model has three kinds of variables: state variables, input variables and parameters. *State variables* describe the physical properties of the medium (velocity, pressure, temperature) and depend on time and space. *Input variables* have to be provided to the model (initial or boundary conditions), most of the time these variables are not directly measured but they can be estimated through data assimilation. Most models contain also a set of *parameters* (e.g. viscosity, thermal diffusivity), which have to be tuned to adjust the model to the observations. All the variables can be polluted by errors.

There are three kinds of systematic errors in numerical modelling of geodynamical problems: model, discretisation and iteration errors. *Model errors* are associated with the idealisation of the Earth’s dynamics by a set of conservation equations governing the dynamics. The model errors are defined as the difference between the actual Earth dynamics and the exact solution of the mathematical model. *Discretisation errors* are defined as the difference between the exact solution of the conservation equations and the exact solution of

the algebraic system of equations obtained by discretising these equations. And *iteration errors* are defined as the difference between the iterative and exact solutions of the algebraic system of equations. It is important to be aware of the existence of these errors, and even more to try to distinguish one from another.

Apart from the errors associated with the numerical modelling, another two components of errors are essential when mantle temperature data are assimilated into the past: (i) data misfit associated with the uncertainties in the present temperature distribution in the Earth's mantle and (ii) errors associated with the uncertainties in initial and boundary conditions. Since there are no direct measurements of mantle temperatures, the temperatures can be estimated indirectly from either seismic wave (and their anomalies), geochemical analysis or through the extrapolation of surface heat flow observations. Many models of mantle temperature are based on the conversion of seismic tomography data into temperature. Meanwhile, a seismic tomography image of the Earth's mantle is a model indeed and incorporates its own model errors. Another source of uncertainty comes from the choice of mantle compositions in the modelling of mantle temperature from the seismic velocities. Therefore, if the present mantle temperature models are biased, information on temperature can be improperly propagated to the geological past.

The temperature at the lower boundary of the model domain used in forward and backward numerical modelling is, of course, an approximation to the real temperature, which is unknown and may change over time at this boundary. Hence, errors associated with the knowledge of the temperature (or heat flux) evolution at the core–mantle boundary are another essential component of errors, which can be propagated into the past during the data assimilation.

In numerical modelling sensitivity analysis assists in understanding the stability of the model solution to small perturbations in input variables or parameters. For instance, if we consider mantle temperature in the past as a solution to the backward model, what will be its variation if there is some perturbation on the inputs of the model (e.g. present temperature data)? The gradient of the objective functional with respect to input parameters in variational data assimilation gives the first-order sensitivity coefficients. The second-order adjoint sensitivity analysis presents some challenge associated with cumbersome computations of the product of the Hessian matrix of the objective functional with some vector (Le Dimet *et al.*, 2002), and hence it is omitted in our study. Hier-Majumder *et al.* (2006) performed first-order sensitivity analysis for two-dimensional problems of thermoconvective flow in the mantle. See Cacuci (2003) and Cacuci *et al.* (2005) for more detail on sensitivity and uncertainty analysis.

- Aiders, M., and U. K. Christensen (1990), The excess temperature of plumes rising from the core-mantle boundary, *Geophys. Res. Lett.*, *23*, 3567–3570.
- Alekseev, A.K. & Navon, I.M., 2001. The analysis of an ill-posed problem using multiscale resolution and second order adjoint techniques, *Comput. Meth. Appl. Mech. Eng.*, *190*, 1937–1953.
- Badro, J., J.-P. Rueff, G. Vanko, G. Monaco, G. Figuet, and F. Guyot (2004), Electronic transitions in perovskite: Possible nonconvecting layers in the lower mantle, *Science*, *305*, 383–386.
- Balla, Z., 1987. Tertiary paleomagnetic data for the Carpatho-Pannonian region in the light of Miocene rotation kinematics. *Tectonophysics* *139*, 67–98.
- Bennett AF. Inverse methods in physical oceanography. Cambridge: Cambridge Univ. Press, 1992.
- Bubnov, V.A., 1976. Wave concepts in the theory of heat, *Int. J. Heat Mass Transfer*, *19*, 175–184.
- Bubnov, V.A., 1981. Remarks on wave solutions of the nonlinear heat conduction equation, *J. Engineering Physics and Thermophysics*, *40(5)*, 907–913.
- Bunge H-P, Richards MA, Lithgow-Bertelloni C, Baumgardner JR, Grand SP, Romanowicz B. Time scales and heterogeneous structure in geodynamic earth models. *Science* 1998; *280*: 91-95.
- Bunge H-P, Richards MA, Baumgardner JR. Mantle circulation models with sequential data-assimilation: Inferring present-day mantle structure from plate motion histories, *Philosophical Transactions of the Royal Society A* 2002; *360*: 2545-2567.
- Bunge, H.-P, Hagelberg, C.R. & Travis, B.J., 2003. Mantle circulation models with variational data assimilation: Inferring past mantle flow and structure from plate motion histories and seismic tomography, *Geophys. J. Int.*, *152*, 280–301.
- Busse, F.H., Christensen, U., Clever, R., Cserepes, L., Gable, C., Giannandrea, E., Guillou, L., Houseman, G., Nataf, H.-C., Ogawa, M., Parmentier, M., Sotin, C., Travis, B., 1993. 3D convection at infinite Prandtl number in Cartesian geometry – a benchmark comparison. *Geophys. Astrophys. Fluid Dyn.* *75*, 39–59.
- Cacuci, D.G., 2003. *Sensitivity and Uncertainty Analysis. Volume I: Theory*, Chapman & Hall / CRC, Boca Raton, 285 p.
- Cacuci, D. G., M. Ionescu-Bujor and I. M. Navon (2005), *Sensitivity and Uncertainty Analysis. Volume II: Applications to Large-Scale Systems*, 368 p., Chapman & Hall/ CRC, Boca Raton.
- Cattaneo, C., 1958. Sur une forme de l'équation de la chaleur éliminant le paradoxe d'une propagation instantanée, *Comptes Rendus*, *247*, 431–433.
- Chandrasekhar, S., 1961. *Hydrodynamic and Hydromagnetic Stability*, Oxford Univ. Press, Oxford, 654 p.
- Chopelas, A., and R. Boehler (1989), Thermal expansion measurements at very high pressure, systematics and a case for a chemically homogeneous mantle. *Geophys. Res. Lett.*, *16*, 1347–1350.
- Cloetingh, S.A.P.L., Burov, E., Matenco, L., Toussaint, G., Bertotti, G., Andriessen, P.A.M., Wortel, M.J.R., Spakman, W., 2004. Thermo-mechanical controls on the Conrad, C.F. & Gurnis, M., 2005. Seismic tomography, surface uplift, and the breakup of Gondwanaland: Integrating mantle convection backwards in time, *Geochem. Geophys. Geosys.*, *4(3)*: doi:10.1029/2001GC000299.
- Csontos, L., Nagymarosy, A., Horvath, F., Kovac, M., 1992. Tertiary evolution of the intra-Carpathian area; a model. *Tectonophysics* *208*, 221–241.
- Daescu, D.N., and Navon, I.M., 2003. An analysis of a hybrid optimization method for variational data assimilation. *Int. J. Comp. Fluid Dyn.*, *17*: 299--306.
- Daudre, B., Cloetingh, S., 1994. Numerical modelling of salt diapirism: influence of the tectonic regime. *Tectonophysics* *240*, 59--79.
- Davaille, A. & Vatteville, J., 2005. On the transient nature of mantle plumes, *Geophys. Res. Lett.*, *32*, L14309, doi:10.1029/2005GL023029.
- Demetrescu, C., Nielsen, S.B., Ene, M., Serban, D.Z., Polonic, G., Andreescu, M., Pop, A., Balling, N., 2001. Lithosphere thermal structure and evolution of the Transylvanian Depression – insight from new geothermal measurements and modelling results. *Phys. Earth Planet. Inter.* *126*, 249–267.
- Le Dimet, F.-X., I. M. Navon, D. N. Daescu (2002), Second-order information in data assimilation, *Mon. Wea. Rev.*, *130*, 629–648
- Forte, A.M. & Mitrovica, J. X., 2001. Deep-mantle high-viscosity flow and thermochemical structure inferred from seismic and geodynamic data, *Nature*, *410*, 1049–1056.
- Fuchs, K., Bonjer, K., Bock, G., Cornea, I., Radu, C., Enescu, D., Jianu, D., Nourescu, A., Merkler, G., Moldoveanu, T., Tudorache, G., 1979. The Romanian earthquake of March 4, 1977. II. Aftershocks and migration of seismic activity. *Tectonophysics* *53*, 225–247.
- Fügenschuh, B., Schmid, S.M., 2005. Age and significance of core complex formation in a very curved orogen: Evidence from fission track studies in the South Carpathians (Romania). *Tectonophysics* *404*, 33–53.
- Girbacea, R., Frisch, W., 1998. Slab in the wrong place: Lower lithospheric mantle delamination in the last stage of the Eastern Carpathian subduction retreat. *Geology* *26*, 611–614.
- Gvirtzman, Z., 2002. Partial detachment of a lithospheric root under the southeast Carpathians: toward a better definition of the detachment concept. *Geology* *30*, 51– 54.
- Hadamard, J., 1902. Sur les problèmes aux dérivées partielles et leur signification physique, *Princeton University Bulletin*, 49–52.
- Hamilton, R.S., 1982. Three manifolds with positive Ricci curvature. *J. Diff. Geom.* *17*, 255–306.
- Hansen, U., D. A. Yuen, and S. E. Kroening (1990), Transition to hard turbulence in thermal convection at infinite Prandtl number, *Phys. Fluids*, *A2(12)*, 2157–2163.
- Hansen, U., D. A. Yuen, and S. E. Kroening (1991), Effects of depth-dependent thermal expansivity on mantle circulations and lateral thermal anomalies, *Geophys. Res. Lett.*, *18*, 1261–1264.
- Hansen, U., D. A. Yuen, S. E. Kroening, and T. B. Larsen (1993), Dynamical consequences of depth-dependent thermal expansivity and viscosity on mantle circulations

- Hier-Majumder, C.A., Belanger, E., DeRosier, S., Yuen, D.A. & Vincent, A.P. (2005). Data assimilation for plume models, *Nonlinear Process in Geophysics*, **12**, 257–267.
- Hier-Majumder, C. A., B. J. Travis, E. Belanger, G. Richard, A. P. Vincent and D. A. Yuen (2006), Efficient sensitivity analysis for flow and transport in the Earth's crust and mantle, *Geophys. J. Int.*, doi: 10.1111/j.1365-246X.2006.02926.x.
- Hofmeister, A. M. (1999), Mantle values of thermal conductivity and the geotherm from photon lifetimes, *Science*, **283**, 1699–1706.
- Honda, S., Morishige, M., Orihashi, Y., 2007. Sinking hot anomaly trapped at the 410 km discontinuity near the Honshu subduction zone, Japan. *Earth Planet. Sci. Lett.* **261**, 565–577.
- Honda, S., S. Balachandar, D. A. Yuen, and D. Reuteler (1993a), Three-dimensional mantle dynamics with an endothermic phase transition, *Geophys. Res. Lett.*, **20**, 221–224.
- Honda, S., D. A. Yuen, S. Balachandar, and D. Reuteler (1993b), Three-dimensional instabilities of mantle convection with multiple phase transitions, *Science*, **259**, 1308–1311.
- Howard, L. N. (1966) Convection at high Rayleigh number, in *Applied Mechanics, Proc. of the 11th Intl Congress of Applied Mechanics, Munich, Germany 1964*, edited by H. Goertler and P. Sorger, pp. 1109–1115, Springer-Verlag, New York.
- Ismail-Zadeh, A.T., Korotkii, A. I., Tsepelev, I.A., 2003a. Numerical approach to solving problems of slow viscous flow backwards in time, in: Bathe, K.J. (Ed.), *Computational Fluid and Solid Mechanics*, Elsevier Science, Amsterdam, pp. 938–941.
- Ismail-Zadeh, A., Mueller, B., Schubert, G., 2005a. Three-dimensional modeling of present-day tectonic stress beneath the earthquake-prone southeastern Carpathians based on integrated analysis of seismic, heat flow, and gravity observations. *Phys. Earth Planet. Inter.* **149**, 81–98.
- Ismail-Zadeh, A., Mueller, B., Wenzel, F., 2005b. Modelling of descending slab evolution beneath the SE-Carpathians: Implications for seismicity, in: Wenzel, F. (Ed.), *Perspectives in Modern Seismology, Lecture Notes in Earth Sciences, Volume 105*, Springer-Verlag, Heidelberg, pp. 205–226.
- Ismail-Zadeh, A.T., Panza, G.F., Naimark, B.M., 2000. Stress in the descending relic slab beneath the Vrancea region, Romania. *Pure Appl. Geophys.* **157**, 111–130.
- Ismail-Zadeh, A.T., Talbot, C.J. & Volozh, Y.A., 2001b. Dynamic restoration of profiles across diapiric salt structures: numerical approach and its applications, *Tectonophysics*, **337**, 21–36.
- Ismail-Zadeh, A.T., Korotkii, A.I., Naimark, B.M., Tsepelev, I.A., 2001a. Numerical modelling of three-dimensional viscous flow under gravity and thermal effects. *Comput. Math. & Math. Phys.* **41**(9), 1331–1345.
- Ismail-Zadeh, A.T., Korotkii, A.I., Naimark, B.M. & Tsepelev, I.A., 2003b. Three-dimensional numerical simulation of the inverse problem of thermal convection, *Comp. Math. & Math. Phys.*, **43**, 587–599.
- Ismail-Zadeh, A., Schubert, G., Tsepelev, I., Korotkii, A., 2004a. Inverse problem of thermal convection: Numerical approach and application to mantle plume restoration. *Phys. Earth Planet. Inter.* **145**, 99–114.
- Ismail-Zadeh, A., Schubert, G., Tsepelev, I., Korotkii, A., 2006. Three-dimensional forward and backward numerical modeling of mantle plume evolution: Effects of thermal diffusion, *J. Geophys. Res.* **111**, B06401, doi:10.1029/2005JB003782.
- Ismail-Zadeh, A., Schubert, G., Tsepelev, I., and Korotkii, A., 2008. Thermal evolution and geometry of the descending lithosphere beneath the SE-Carpathians: An insight from the past, *Earth and Planetary Science Letters*, **273**: 68-79.
- Ismail-Zadeh, A.T., Tsepelev, I.A., Talbot, C.J. & Korotkii, A.I., 2004b. Three-dimensional forward and backward modelling of diapirism: Numerical approach and its applicability to the evolution of salt structures in the Pricaspian basin, *Tectonophysics*, **387**, 81–103.
- Ismail-Zadeh, A. T., Tsepelev, I. A., Talbot, C. J., Oster, P., 2000. A numerical method and parallel algorithm for three-dimensional modeling of salt diapirism. In: Keilis-Borok, V. I., Molchan, G. M. (Eds.) *Problems in Dynamics and Seismicity of the Earth*. GEOS, Moscow, pp. 62--76.
- Jackson, M. P. A., Vendeville, B. C., and Schultz-Ela, D. D., 1994, Structural dynamics of salt systems. *Annual Review of Earth and Planetary Sciences* **22**, 93-117.
- Jiricek, R., 1979. Tectonic development of the Carpathian arc in the Oligocene and Neogene, in: Mahel, M. (Ed.), *Tectonic Profiles Through the Western Carpathians*, Geol. Inst., Dionyz Stur, pp. 205–214.
- Kalnay, E., 2003. *Atmospheric Modeling, Data Assimilation and Predictability*, Cambridge Univ. Press, Cambridge, 341 p.
- Karato, S.-I., 1993. Importance of anelasticity in the interpretation of seismic tomography. *Geophys. Res. Lett.* **20**, 1623–1626.
- Katsura, T., Yamada, H., Nishikawa, O., Song, M., Kubo, A., Shinmei, T., Yokoshi, S., Aizawa, Y., Yoshino, T., Walter, M.J., Ito, E. & Funakoshi, K., 2004. Olivine-wadsleyite transition in the system (Mg, Fe)₂SiO₄, *J. Geophys. Res.*, **109**, B02209, doi:10.1029/2003JB002438.
- Kaus, B.J.P. & Podladchikov, Y.Y., 2001. Forward and reverse modeling of the three-dimensional viscous Rayleigh-Taylor instability, *Geophys. Res. Lett.*, **28** (6), 1095–1098.
- van Keken, P.E., Spiers, C. J., van den Berg, A. P., Muzyert, E. J., 1993. The effective viscosity of rocksalt: implementation of steady-state creep laws in numerical models of salt diapirism. *Tectonophysics* **225**, 457-476.
- Kirsch, A., 1996. *An Introduction to the Mathematical Theory of Inverse Problems*, Springer-Verlag, New York, 282 pp.
- Korotkii, A. I., and I. A. Tsepelev (2003), Solution of a retrospective inverse problem for one nonlinear evolutionary model, in *Proc. of the Steklov Institute of Mathematics, Suppl. 2*, pp. 80-94, MAIK, Moscow.
- Korotkii, A. I., Tsepelev, I. A., Ismail-Zadeh, A. T. & Naimark, B. M., 2002. Three-dimensional backward modeling in problems of Rayleigh-Taylor instability.

- salt tectonics. Geological Society Special Publication 100, London, pp. 243-258.
- Lattes, R. & Lions, J.L., 1969. *The Method of Quasi-Reversibility: Applications to Partial Differential Equations*, Elsevier, New York, 388 p.
- Leitch, A. M., V. Steinbach, and D. A. Yuen (1996), Centerline temperature of mantle plumes in various geometries: Incompressible flow, *J. Geophys. Res.*, *101*, 21829–21846.
- Linzer, H.-G., 1996. Kinematics of retreating subduction along the Carpathian arc, Romania. *Geology* *24*, 167–170.
- Liu, D. C. and J. Nocedal (1989), On the limited memory BFGS method for large scale optimization, *Math. Programming*, *45*, 503-528.
- Liu L, Gurnis M. Simultaneous inversion of mantle properties and initial conditions using an adjoint of mantle convection. *Journal of Geophysical Research* 2008; *113*: B08405, doi:10.1029/2008JB005594.
- Liu, M., D. A. Yuen, W. Zhao, and S. Honda (1991), Development of diapiric structures in the upper mantle due to phase transitions, *Science*, *252*, 1836–1839.
- Malevsky, A. V., and D. A. Yuen (1993), Plume structures in the hard-turbulent regime of three-dimensional infinite Prandtl number convection, *Geophys. Res. Lett.*, *20*, 383–386.
- Malevsky, A. V., D. A. Yuen, and L. M. Weyer (1992), Viscosity and thermal fields associated with strongly chaotic non-Newtonian thermal convection, *Geophys. Res. Lett.*, *19*, 127–130.
- Martin, M., Ritter, J.R.R., the CALIXTO working group, 2005. High-resolution teleseismic body-wave tomography beneath SE Romania – I. Implications for three-dimensional versus one-dimensional crustal correction strategies with a new crustal velocity model. *Geophys. J. Int.* *162*, 448–460.
- Martin, M., Wenzel, F., the CALIXTO working group, 2006. High-resolution teleseismic body wave tomography beneath SE-Romania – II. Imaging of a slab detachment scenario: *Geophys. J. Int.* *164*, 579–595.
- McKenzie, D. P., 1972. Active tectonics of the Mediterranean region. *Geophys. J. Roy. Astr. Soc.* *30*, 109–185.
- McLaughlin D. An integrated approach to hydrologic data assimilation: Interpolation, smoothing, and forecasting. *Advances in Water Resources* 2002; *25*: 1275–1286.
- Boussinesq, J., 1903. *Theorie Analytique de la Chaleur*, Vol. 2, Gauthier-Villars, Paris, 172 pp.
- Mitrovica, J. X. (1996), Haskell (1935) revisited, *J. Geophys. Res.*, *101*, 555–569.
- Mitrovica, J. X., and A. M. Forte (2004), A new inference of mantle viscosity based upon joint inversion of convection and glacial isostatic adjustment data, *Earth Planet. Sci. Lett.*, *225*, 177–189.
- Montelli, R., Nolet, G., Dahlen, F.A., Masters, G., Engdahl, E.R. & Hung, S.-H., 2004. Finite-frequency tomography reveals a variety of plumes in the mantle, *Science*, *303*, 338–343.
- Moore, W. B., Schubert, G. & Tackley, P., 1998. Three-dimensional simulations of plume–lithosphere interaction at the Hawaiian Swell, *Science*, *279*, 1008–1011.
- Morgan, W. J. (1972), Plate motions and deep convection, or the outer Carpathian thrust sheets. *Tectonics* *15*, 885–904.
- Morra, G., Regenauer-Lieb, K., Giardini, D., 2006. Curvature of oceanic arcs. *Geology* *34*, 877–880.
- Morse, P.M. & Feshbach, H., 1953. *Methods of Theoretical Physics*, McGraw-Hill, New York, 865 p.
- Naimark, B. M., Ismail-Zadeh, A. T., Jacoby, W. R., 1998. Numerical approach to problems of gravitational instability of geostructures with advected material boundaries. *Geophysical Journal International* *134*, 473–483.
- Nitoi, E., Munteanu, M., Marincea, S., Paraschivoiu, V., 2002. Magma-enclave interactions in the East Carpathian Subvolcanic Zone, Romania: petrogenetic implications. *J. Volcan. Geother. Res.* *118*, 229–259.
- Nolet, G., and F. A. Dahlen (2000), Wave front healing and the evolution of seismic delay times, *J. Geophys. Res.*, *105*, 19043–19054.
- Olson, P., and H. Singer (1985), Creeping plumes, *J. Fluid Mech.*, *158*, 511–531.
- Oncescu, M.C., 1984. Deep structure of the Vrancea region, Romania, inferred from simultaneous inversion for hypocentres and 3-D velocity structure. *Ann. Geophys.* *2*, 23–28.
- Oncescu, M.C., Bonjer, K.P., 1997. A note on the depth recurrence and strain release of large Vrancea earthquakes. *Tectonophysics* *272*, 291–302.
- Pana, D., Erdmer, P., 1996. Kinematics of retreating subduction along the Carpathian arc, Romania: Comment. *Geology* *24*, 862–863.
- Pana, D., Morris, G.A., 1999. Slab in the wrong place: Lower lithospheric mantle delamination in the last stage of the Eastern Carpathian subduction retreat: Comment. *Geology* *27*, 665–666.
- Perelman, G., 2002. The entropy formula for the Ricci flow and its geometric applications, <http://arxiv.org/abs/math.DG/0211159>.
- Poliakov, A. N. B., van Balen, R., Podladchikov, Yu., Daudre, B., Cloetingh, S., Talbot, C., 1993a. Numerical analysis of how sedimentation and redistribution of surficial sediments affects salt diapirism. *Tectonophysics* *226*, 199–216.
- Poliakov, A. N. B., Podladchikov, Yu., Talbot, C., 1993b. Initiation of salt diapirs with frictional overburdens: numerical experiments. *Tectonophysics* *228*, 199–210.
- Poliakov, A., Podladchikov, Yu., Dawson, E., Talbot, C., 1996. Salt diapirism with simultaneous brittle faulting and viscous flow. In: Alsop, I., Blundell, D., Davison, I. (Eds.) *Salt Tectonics*. Geological Society Special Publication No. 100, London, pp. 291–302.
- Popa, M., Radulian, M., Grecu, B., Popescu, E., Placinta, A.O., 2005. Attenuation in Southeastern Carpathians area: Result of upper mantle inhomogeneity. *Tectonophysics* *410*, 235–249.
- Ramberg, H., 1968. Instability of layered system in the field of gravity. *Physics of the Earth and Planetary Interiors* *1*, 427–474.
- Ribe, N.M. & Christensen, U., 1994. Three-dimensional modeling of plume-lithosphere interaction, *J. Geophys. Res.*, *99*, 669–682.
- Richards, M. A., R. A. Duncan, and V. Courtillot (1989),

- for heat flux, *Science*, 290, 515–516.
- Royden, L.H., 1988. Late Cenozoic tectonics of the Pannonian basin system, *Am. Assoc. Petrol. Geol. Mem.* 45, 27–48.
- Römer, M.-M., Neugebauer, H. J., 1991. The salt dome problem: A multilayered approach. *Journal of Geophysical Research* 96, 2389–2396.
- Samarskii, A.A. & Vabishchevich, P.N., 1995. *Computational Heat Transfer. Vol. 1. Mathematical Modelling*, John Wiley & Sons, New York, 370 p.
- Samarskii, A.A. & Vabishchevich, P.N., 2004. *Numerical Methods for Solving Inverse Problems of Mathematical Physics*, URSS, Moscow, 478 p (in Russian).
- Samarskii, A.A., Vabishchevich, P.N. & Vasiliev, V.I., 1997. Iterative solution of a retrospective inverse problem of heat conduction, *Math. Modeling*, 9(5), 119–127.
- Sandulescu, M., 1988. Cenozoic Tectonic History of the Carpathians, *Am. Assoc. Petrol. Geol. Mem.* 45, 17–25.
- Schmeling, H., 1987. On the relation between initial conditions and late stages of Rayleigh-Taylor instabilities. *Tectonophysics* 133, 65–80.
- Schubert, G., Turcotte, D.L., and Olson, P., 2001. *Mantle Convection in the Earth and Planets*. Cambridge University Press, Cambridge, 940 pp.
- Seghedi, I., Downes, H., Vaselli, O., Szakacs, A., Balogh, K., Pecskey, Z., 2004. Post-collisional Tertiary-Quaternary mafic alkalic magmatism in the Carpathian-Pannonian region: a review. *Tectonophysics* 393, 43–62.
- Sleep, N. H. (1990). Hotspots and mantle plumes: some phenomenology, *J. Geophys. Res.*, 95, 6715–6736.
- Sperner, B., the CRC 461 Team, 2005. Monitoring of slab detachment in the Carpathians, in: Wenzel, F. (Ed.), *Challenges for Earth Sciences in the 21st Century*. Springer-Verlag, Heidelberg, pp. 187–202.
- Sperner, B., Lorenz, F., Bonjer, K., Hettel, S., Müller, B., Wenzel, F., 2001. Slab break-off – abrupt cut or gradual detachment? New insights from the Vrancea region (SE Carpathians, Romania). *Terra Nova* 13, 172–179.
- Stanica, D., Stanica, M., 1993. An electrical resistivity lithospheric model in the Carpathian orogen from Romania. *Phys. Earth Planet. Inter.* 81, 99–105.
- Steinberger, B. & O'Connell, R.J., 1998. Advection of plumes in mantle flow: implications for hotspot motion, mantle viscosity and plume distribution, *Geophys. J. Int.*, 132, 412–434.
- Szabó, C., Falus, G., Zajacz, Z., Kovacs, I., Bali, E., 2004. Composition and evolution of lithosphere beneath the Carpathian-Pannonian Region: a review. *Tectonophysics* 393, 119–137.
- Talbot, C. J., 1995. Molding of salt diapirs by stiff overburdens. In: Jackson, M.P.A., Roberts, D.G., Snelson, S. (Eds.) *Salt Tectonics - A Global Perspective*. American Association of Petroleum Geologists. Memoir 65, Tulsa, pp. 61–75.
- Tarapouca, M., Carcia-Catellanos, D., Bertotti, G., Matenco, L., Cloetingh, S.A.P.L., Dinu, C., 2004. Role of the 3-D distributions of load and lithospheric strength in orogenic arcs: polystage subsidence in the Carpathians foredeep. *Earth Planet. Sci. Lett.* 221, 163–180.
- Tikhonov, A.N., 1963, Solution of incorrectly formulated problems and the regularization method, *Doklady* ИКНОПОВ, А.Н. & Самарский, А.А., 1990. *Equations of Mathematical Physics*, Dover Publications, New York, 765 pp.
- Trompert, R. A., and U. Hansen (1998), On the Rayleigh number dependence of convection with a strongly temperature-dependent viscosity, *Phys. Fluids*, 10, 351–360.
- Vasiliev, F.P., 2002. *Methody optimizatsii*. Factorial Press, Moscow, 824 pp (in Russian).
- Vendeville, B. C., Jackson, M. P. A., 1992. The rise of diapirs during thin-skinned extension. *Marine and Petroleum Geology* 9, 331–353.
- Vernotte, P., 1958. Les paradoxes de la theorie continue de l'equation de la chaleur, *Comptes Rendus*, 246, 3154–3155.
- Weidle, C., Wenzel, F., Ismail-Zadeh, A., 2007. t^* - an unsuitable parameter for anelastic attenuation in the Eastern Carpathians. *Geophys. J. Int.* 170, 1139–1150.
- Woidt, W.-D., 1978. Finite element calculations applied to salt dome analysis. *Tectonophysics* 50, 369–386.
- Wortel, M.J.R., Spakman, W., 2000. Subduction and slab detachment in the Mediterranean-Carpathian region. *Science* 290, 1910–1917.
- Yu, N., Imatani, S. & Inoue, T., 2004. Characteristics of temperature field due to pulsed heat input calculated by non-Fourier heat conduction hypothesis, *JSME Int. J., Series A*, 47(4), 574–580.
- Zhong, S. (2005), Dynamics of thermal plumes in three-dimensional isoviscous thermal convection, *Geophys. J. Int.*, 162, 289–300.
- Zou, X., I. M. Navon, M. Berger, K. H. Phua, T. Schlick and F. X. Le Dimet (1993), Numerical experience with limited-memory quasi-Newton and truncated Newton methods, *SIAM J. Optimization*, 3(3), 582–608.